Bioactive Materials 41 (2024) 523–536

Contents lists available at ScienceDirect

Bioactive Materials

journal homepage: www.keaipublishing.com/en/journals/bioactive-materials

Plant-inspired visible-light-driven bioenergetic hydrogels for chronic wound healing

Yuping Jiang [a,b], Xiaomin Feng [a,b], Xin Qiao [a,b], Yufeng Li [a,b], Xiaozhuang Li [a,b], Jinguang Yang [c], Lu Han [a,b,*]

[a] Key Laboratory of Marine Drugs, Ministry of Education, School of Medicine and Pharmacy, Ocean University of China, Qingdao, 266003, China
[b] Laboratory for Marine Drugs and Bioproducts, Qingdao Marine Science and Technology Center, Qingdao, 266237, China
[c] Key Laboratory of Tobacco Pest Monitoring & Integrated Management, Tobacco Research Institute of Chinese Academy of Agricultural Sciences, Qingdao, 266101, China

ARTICLE INFO

Keywords:
Polyphenol nanoparticles
Photosynthetic thylakoid
Inflammation regulation
Diabetic wound repairing
Hydrogel

ABSTRACT

Chronic bioenergetic imbalances and inflammation caused by hyperglycemia are obstacles that delay diabetic wound healing. However, it is difficult to directly deliver energy and metabolites to regulate intracellular energy metabolism using biomaterials. Herein, we propose a light-driven bioenergetic and oxygen-releasing hydrogel (PTKM@HG) that integrates the thylakoid membrane-encapsulated polyphenol nanoparticles (PTKM NPs) to regulate the energy metabolism and inflammatory response in diabetic wounds. Upon red light irradiation, the PTKM NPs exhibited oxygen generation and H_2O_2 deletion capacity through a photosynthetic effect to restore hypoxia-induced mitochondrial dysfunction. Meanwhile, the PTKM NPs could produce exogenous ATP and NADPH to enhance mitochondrial function and facilitate cellular anabolism by regulating the leucine-activated mTOR signaling pathway. Furthermore, the PTKM NPs inherited antioxidative and anti-inflammatory ability from polyphenol. Finally, the red light irradiated PTKM@HG hydrogel augmented the survival and migration of cells keratinocytes, and then accelerated angiogenesis and re-epithelialization of diabetic wounds. In short, this study provides possibilities for effectively treating diseases by delivering key metabolites and energy based on such a light-driven bioenergetic hydrogel.

1. Introduction

As a common complication of diabetes, the diabetic wound healing process involves prolonged inflammation, insufficient angiogenesis, and ultimately delayed healing owing to the pathological microenvironment accompanied by oxidative stress and bioenergetic imbalance caused by hyperglycemia [1–5]. Under hyperglycemic conditions, the oxygen consumption and energy demand of cells are elevated, and defective blood vessels at wound sites impede oxygen delivery, exacerbating the hypoxic environment [6–9]. Hypoxic and hyperglycemic conditions induce the overproduction of mitochondrial reactive oxygen species (ROS), which exceeds cellular self-antioxidant defenses, leading to a state of oxidative stress that fuels inflammation and disrupts mitochondrial redox homeostasis [10–13]. Mitochondria function as ROS amplifiers that initiate further ROS release in neighboring mitochondria, resulting in widespread mitochondrial dysfunction and a subsequent bioenergetic imbalance with decreased adenosine triphosphate (ATP) generation, which is suggested to play a central role in cellular anabolism during cell differentiation and proliferation [14,15]. Thus, the restoration of mitochondrial functions, including energy production and redox homeostasis, has been identified as a potential target for promoting tissue regeneration in diabetic wounds [16–18].

Increased ROS levels disrupt redox homeostasis, and long-term hypoxia results in the recruitment and accumulation of inflammatory cells (M1 macrophages) [19–22]. M1 macrophages are enriched in the early inflammatory sites and activated by pro-inflammatory factors such as lipopolysaccharide (LPS) and IFN-γ, and then prolong inflammatory response by secreting inflammatory factors, which can seriously inhibit angiogenesis, tissue repair and tissue structure reconstruction [23–26]. Disorders in cellular metabolism, especially amino acid and energy metabolism, inhibit macrophage activation and weaken the adaptability of macrophages, which can inhibit long-term tissue remodeling in

Peer review under responsibility of KeAi Communications Co., Ltd.
* Corresponding author. Key Laboratory of Marine Drugs, Ministry of Education, School of Medicine and Pharmacy, Ocean University of China, China.
E-mail address: hanlu@ouc.edu.cn (L. Han).

https://doi.org/10.1016/j.bioactmat.2024.08.003
Received 11 March 2024; Received in revised form 25 June 2024; Accepted 5 August 2024
2452-199X/© 2024 The Authors. Publishing services by Elsevier B.V. on behalf of KeAi Communications Co. Ltd. This is an open access article under the CC BY-NC-ND license (http://creativecommons.org/licenses/by-nc-nd/4.0/).

chronic diabetic wounds [27–30]. Protecting mitochondria to reduces the level of oxidative stress, regulates the balance of cell metabolism and thus reduces the inflammatory response, which can also regulate the pathological microenvironment and play an important role in reversing chronic diabetic wounds [28,31–33]. Therefore, exploring a comprehensive treatment model that protects mitochondria from damage and corrects metabolic disorders will fundamentally accelerate the healing process of chronic wounds [18,34–36]. However, direct regulation of intracellular metabolism via biomaterials remains challenging owing to the unsatisfactory delivery of energy and metabolites [37–39].

Natural biological systems derived from plants have been widely studied as therapeutic agents because they are green, sustainable and highly biosafe [40]. For example, plant leaves [41], algae [42,43], and bacteria [10] exhibit remarkable biosynthetic capacity by absorbing sunlight and converting it into vital chemical energy via photosynthesis [41]. Especially, the PS-I and PS-II systems in the thylakoid membrane of plant leaves can not only effectively catalyze water into oxygen upon sunlight irradiation, but also produce abundant ATP and nicotinamide adenine dinucleotide phosphate (NADPH), which can serve as energy supplier to promote and regulate mitochondrial functions. In addition, natural polyphenols, such as tannic acid [44,45], resveratrol [46] and curcumin [47,48], realize anti-inflammatory and antioxidative functions. Therefore, the combination of naturally derived living biological systems can endow artificial systems with complex functions that promote biological therapy.

Herein, by taking advantage of the plant-derived photosynthetic thylakoid membrane (TKM) and ROS-scavenging polyphenol nanoparticles (NPs), we developed photosynthetic PTKM NPs by coating poly-tannic acid (PTA) NPs with the TKM derived from spinach, and then incorporated the PTKM NPs into oxidized hyaluronic acid (OHA) and amino-modified gelatin (Gel-NH_2) based matrix to form a light-driven bioenergetic and oxygen-releasing hydrogel (designated as PTKM@HG) (Scheme 1a). When applied to diabetic wound, the acidic microenvironment induces the degradation of the hydrogel, thereby locally releasing PTKM NPs to the wound sites. Under natural-light or red-light irradiation, the PTKM NPs can not only continuously generate photocatalytic water to generate oxygen, but also induce NADH and ADP reduction to yield exogenous NADPH and ATP through the photosynthetic effect. Therefore, PTKM NPs restored mitochondrial function and enhanced mitochondrial function by supplying oxygen, NADPH, and ATP, which corrected impaired metabolism and augmented the survival and migration of endothelial cells and keratinocytes. Meanwhile, PTKM NPs inherited antioxidative and anti-inflammatory properties from PTA NPs with abundant polyphenol

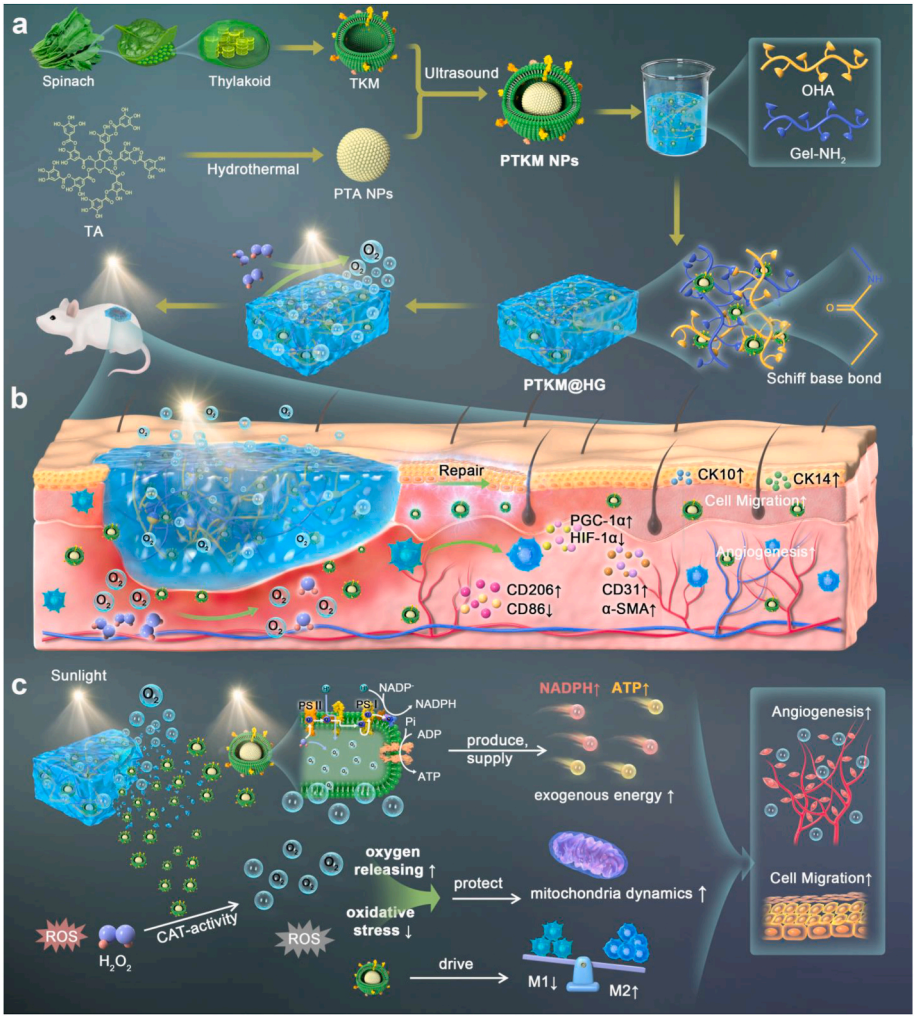

Scheme 1. Schematic illustration of visible light-driven bioenergetic and oxygen-releasing hydrogel for accelerating wound healing under light irradiation. (a) Schematic diagram of the procedure for fabricating PTKM NPs and PTKM@HG hydrogel. (b) Applications of the PTKM@HG hydrogel in wound healing. (c) Promoting wound healing mechanisms of PTKM@HG upon visible light irradiation, including scavenging ROS to protect cells from oxidative stress, generating oxygen to greatly alleviate hypoxia, correcting mitochondrial dynamics, enhancing cell metabolism by supplying sufficient ATP and NADPH through the photosynthesis process to regulate the hyperglycemia-induced microenvironments and finally promote cell migration and angiogenesis.

groups, which scavenged ROS and suppressed the ROS-induced inflammatory response to drive the healing process to the regenerative phases. The prominent photosynthetic features of the PTKM NPs endowed the hydrogel with the ability to regulate hyperglycemia-induced oxidative stress, hypoxia, inflammation, and metabolic disorders via light-driven supplementation with exogenous energy and metabolites for diabetic wound healing (Scheme 1b and c).

2. Results and discussion

2.1. Fabrication and characterizations of PTKM NPs

The synthesis procedure for the PTKM NPs is illustrated in Scheme 1a. Thylakoids were harvested from spinach by differential centrifugation [49]. TKM (2.45 mg/mL) was obtained by ultracentrifugation, washing, and ultrasonication. As shown in the transmission electron microscopy (TEM) image, the extracted TKM exhibit a completely layered structure (Fig. 1a). Next, PTA NPs were obtained from tannic acid (TA) via formaldehyde cross-linking and the hydrothermal method [50], displayed a monodispersed spherical structure with a diameter of 245 nm and a rough surface (Fig. 1b and Fig. S1). Fourier transform infrared (FTIR) spectroscopy provided additional evidence for the successfully preparation of PTA NPs. In contrast to the spectra of unmodified TA, distinct absorption peaks appeared at 2930 cm^{-1} in the spectra of PTA NPs (Fig. S2), corresponding to the $–CH_2-$ vibration, confirming the effective incorporation of the $–CH_2-$ groups derived from formaldehyde through phenol-formaldehyde condensation into the PTA NPs [51]. Finally, PTA NPs were mixed with TKM vesicles under ultrasonication to construct TKM-coated PTA NPs, denoted as PTKM NPs. It was noted that PTA NPs with a negative charge were conducive to encapsulation by biological cell membranes with inherent charge asymmetry without damaging the structural integrity and fluidity of the membranes [52], which could retain the biological activity of TKM. The distinct core-shell structure from TEM observation revealed the successful formation of PTKM NPs (Fig. 1c and d). The size distribution results indicated that the PTKM NPs had a diameter of approximately ~263 nm (Fig. S3), and the zeta potential of the PTKM NPs was similar to that of the original TKM (Fig. 1e), confirming the encapsulation of PTA NPs by TKM. X-ray photoelectron spectroscopy (XPS) spectrum indicated the binding energy peaks of PTKM NPs at 284.8 eV, 531.91 eV and 133.15 eV, corresponding to C1s, O1s, and P2p, respectively (Fig. 1f and Fig. S4). The high-resolution O1s peaks of the PTKM NPs were fitted with three distinct peaks at 531.25 eV, 532.2 eV, and 536.25 eV in the O1s spectrum, representing the C=O, C-O and C-OH components in PTA NPs, respectively (Fig. 1g). The detection of P2p at 133.15 eV indicated the presence of TKM (Fig. 1h). Membrane proteins of the PTKM NPs were analyzed using blue native polyacrylamide gel electrophoresis (BN-PAGE), which confirmed the presence of specific photosynthetic activity-related membrane proteins, including photosynthetic system I (PS-I), photosynthetic system II (PS-II) and light-harvesting complex II (LHC-II) on the PTKM NPs (Fig. 1i). Furthermore, the adsorption peak around 665 nm appeared in the ultraviolet–visible (UV–Vis) spectra of PTKM NPs but not in PTA NPs (Fig. 1j), which was the typical absorption of chlorophylls in TKM. Together, these results demonstrated the successful fabrication of PTKM NPs using the PS-I/PS-II system for photosynthesis.

To verify the photosynthetic efficiency of PTKM NPs, their oxygenation capacity was evaluated using a dissolved oxygen meter under sunlight and 660 nm LED irradiation. PTKM NPs could continually produce oxygen upon exposure to sunlight, and the oxygen level reached above 0.69 mg/L after 130 s (Fig. 1k). Moreover, the oxygen levels exceeded 1.0 mg/L after 12 min of LED irradiation (Fig. 1l). Additionally, PTKM NPs possessed catalase activity that can catalyze hydrogen peroxide (H_2O_2) to produce oxygen (O_2) under 660 nm LED irradiation, which plays a key role in relieving hypoxia at diabetic wound sites. As shown in Fig. 1m, the content of O_2 was significantly elevated in the

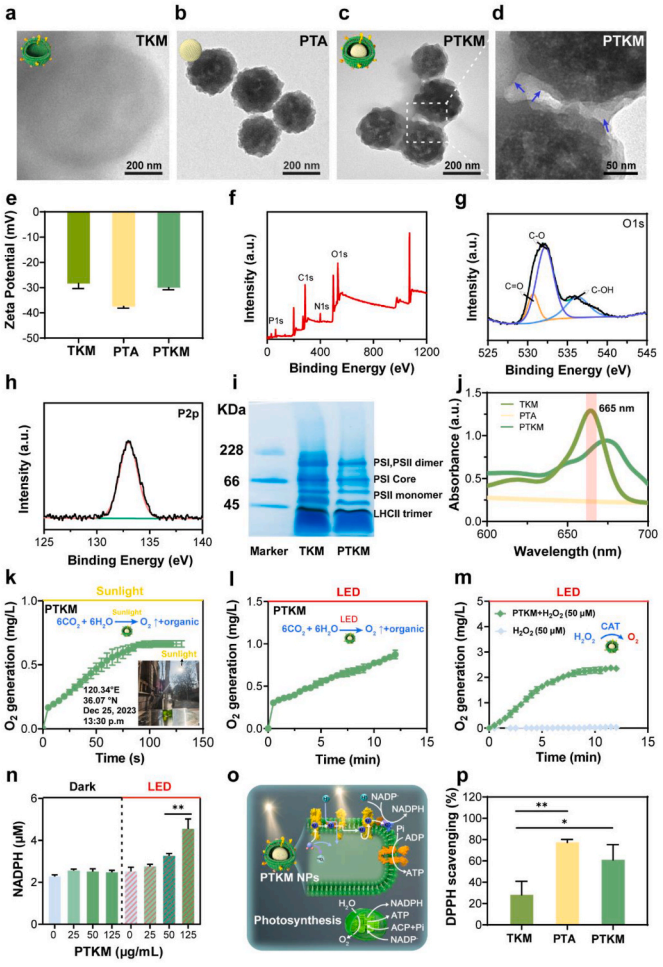

Fig. 1. Fabrication and characterizations of PTKM NPs. TEM images of (a) thylakoid membranes (TKM), (b) PTA NPs, (c) and (d) PTKM NPs. Arrows (blue) refer to the thylakoid membrane. (e) Zeta potentials of TKM, PTA and PTKM NPs. (f) XPS survey spectra of PTKM NPs. (g) High resolution XPS spectra of O1s for PTKM NPs. (h) High resolution XPS spectra of P2p for PTKM NPs. (i) Blue native polyacrylamide gel (BN-PAGE) electrophoresis of TKM and PTKM NPs. (j) UV–Vis absorption spectra of TKM, PTA and PTKM NPs. (k) Photosynthesis ability of PTKM NPs under sunlight, insert shows the photo of the experimental setup. (l) Photosynthesis ability of PTKM NPs under 660 nm LED irradiation. (m) CAT-like activity of different groups (PTKM NPs+ 50 μM H_2O_2) under 660 nm LED irradiation. (n) NADPH production ability of PTKM NPs in the presence and absence of LED irradiation. (o) Schematic diagram of the mechanism of PTKM involved in photosynthesis. (p) DPPH scavenging efficiency of different nanomaterials. *$p < 0.05$, **$p < 0.01$. The data are presented as the mean ± s.d. ($n = 3$).

PTKM NPs solution upon adding H_2O_2 (50 μM). In addition, duration tests demonstrated that the PTKM NPs exhibited stable photosynthetic effect to continuously generate oxygen during the two cycles of on/off LED irradiation (Fig. S5).

The ability of PTKM NPs to product NADPH under light irradiation was assessed using the WST-8 assay under dark and light-irradiation conditions (Fig. 1n). In this system, light irradiation induces electron transfer, from stromal ferredoxin (Fd) to ferredoxin-nicotinamide adenine dinucleotide phosphate (NADP) oxidoreductase (FNR), enabling the reduction of NADP + to NADPH. The fold change yield of NADPH formation is 199.60 % for PTKM NPs with the concertation at 125 μg/mL. For comparison, the inefficient generation of NADPH was observed under dark conditions. These results confirmed that PTKM NPs retained the natural structure and photosynthetic performance of TKM, which served as an energy supplier to promote and regulate cellular

functions under light irradiation (Fig. 1o).

Additionally, PTKM NPs possessed excellent the antioxidant ability inherited from PTA NPs, as demonstrated by the classic 1-diphenyl-2-picrylhydrazyl (DPPH) radical assay. The UV–Vis spectra revealed that the absorbance at 517 nm decreased for PTA and PTKM NPs (Fig. S6). After 90 min of incubation, more than 70 % of the DPPH free radicals were eliminated by the PTA NPs (Fig. 1p). Together, these results revealed that PTKM NPs can be used as an all-in-one nanoplatform with photosynthetic oxygen/energy evolution and free radical scavenging abilities to regulate disordered metabolism in diabetic wounds under light illumination.

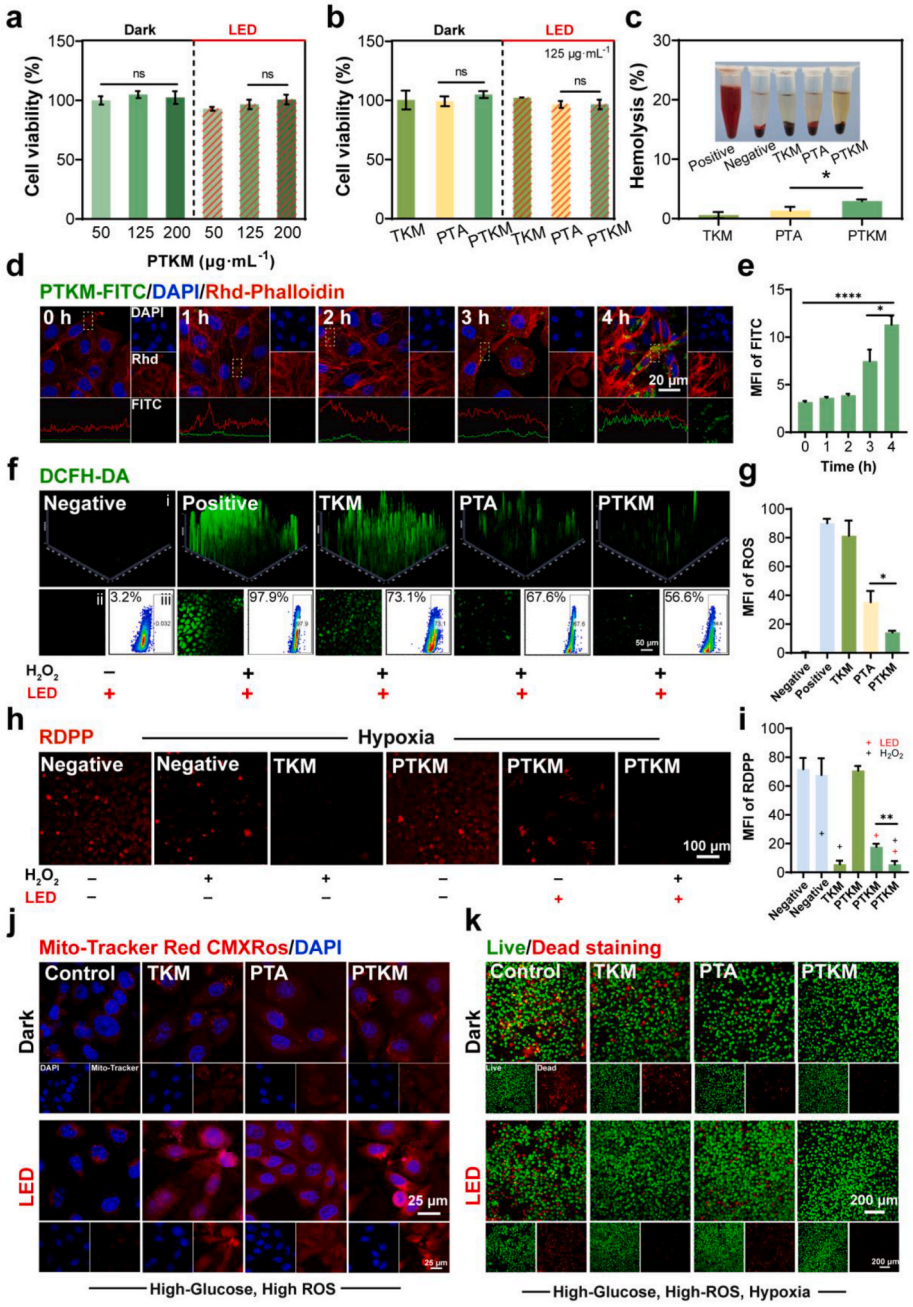

Fig. 2. The protective ability of PTKM NPs on HUVECs cultured under high ROS, hypoxic and high-glucose conditions to mimic the in vivo microenvironment. (a) and (b) Viability of HUVECs after co-incubation with different concentrations of PTKM NPs and different nanomaterials for 6 h. The time for LED irradiation was 30 min. (c) Hemolysis ratios of TKM, PTA and PTKM NPs (37 °C, incubation time: 4 h), insert shows the hemolysis photo. (d) Cellular uptake of FITC-labeled PTKM NPs at 0, 1, 2, 3 and 4 h in HUVECs. Nuclei were stained with DAPI (blue) and F-actin was stained with Rhodamine-labeled phalloidin (red). (e) Mean fluorescence intensity (MFI) analysis of PTKM NPs uptake at different times. (f) Fluorescence images (CLSM images and 2.5 D fluorescence images) and flow cytometry illustrating intracellular ROS in 50 μM H_2O_2-stimulated HUVECs incubated with different nanoparticles under 660 nm irradiation (20 W) for 30 min. (g) Mean fluorescence intensity (MFI) analysis of ROS. (h) Intracellular oxygen generation in HUVECs incubated with different nanoparticles under high ROS and hypoxic conditions detected by RDPP. (i) MFI analysis of fluorescence signals in (h). (j) Mito-Tracker Red CMXRos images of mitochondrial potential stained in HUVECs incubated with different nanoparticles under high glucose and ROS conditions. (k) Live/dead staining of HUVECs incubated with different nanoparticles under high glucose, high ROS, and hypoxic conditions. *$p < 0.05$, **$p < 0.01$, ****$p < 0.0001$. The data are presented as the mean ± s.d. ($n = 3$).

2.2. Cytocompatibility and hemolysis evaluations of PTKM NPs

Before evaluating the in vitro bioactivity, the cytocompatibility of PTKM NPs was evaluated using human umbilical vein endothelial cells (HUVECs). As shown in Fig. 2a, the cell counting kit 8 (CCK-8) assay demonstrated that the cell proliferation and survival rate of HUVECs were not affected even at the high concentration of PTKM NPs (200 μg/mL). In addition, there was no difference in cell viability among the groups after 6 h of co-culture with different nanomaterials (TKM, PTA and PTKM NPs) (Fig. 2b). The LED irradiation resulted in negligible toxicity. Moreover, PTKM NPs displayed a low hemolysis ratio (5 %), indicating excellent blood compatibility (Fig. 2c). Next, the uptake efficiency of HUVECs and the intracellular distribution were monitored using fluorescein isothiocyanate (FITC) -labeled PTKM NPs (PTKM-FITC). As shown in Fig. 2d–e and Fig. S7, increased incubation time from 1 h to 4 h resulted in a significant increase in fluorescence intensity, indicating that the PTKM NPs can be endocytosed by HUVECs to exert their function inside cells. In addition, representative fluorescence images of the mitochondria and PTKM-FITC NPs demonstrated that PTKM NPs were centralized around the mitochondria (Fig. S8), which was favorable for the regulation of mitochondrial function by PTKM NPs.

2.3. Cytoprotective ability of PTKM NPs under high ROS, high-glucose and hypoxic conditions

To evaluate the cytoprotective ability of PTKM NPs in complex diabetic wounds, we conducted a series of in vitro experiments under high ROS, high-glucose, and hypoxic conditions to mimic the in vivo pathological microenvironment. First, the ROS scavenging ability of the PTKM NPs was conducted by incubating HUVECs with 125 μg/mL PTKM NPs, followed by H_2O_2 (50 μM) treatment, and then the intracellular ROS level was investigated by the fluorescence signal of the DCFH-DA probe using confocal laser scanning microscopy (CLSM) and flow cytometry (Fig. 2f). Compared to the H_2O_2 treated-positive group, the intracellular ROS level was slightly decreased in the TKM + LED-treated group, which was due to the CAT activity of TKM catalyzed hydrogen peroxide upon light irradiation [53]. Intracellular ROS levels were reduced by PTA and PTKM NPs, which was attributed to the reductive phenolic groups on PTA NPs that acted as electron donors and interacted with radicals [54–56]. Quantitative analysis of intracellular ROS levels by flow cytometry further confirmed this observation (Fig. 2g). The above results demonstrated that the CAT activity of TKM and the polyphenolic groups from PTA NPs synergistically endowed PTKM NPs with an excellent antioxidative ability to scavenge ROS and therefore protect cells from pathological oxidative stress.

Next, the oxygen generation capacity of PTKM NPs in HUVECs was examined by the in vitro oxidative and hypoxia model (50 μM H_2O_2, 5 % O_2). The $[Ru(dpp)_3]Cl_2$ probe (RDPP) was used to evaluate intracellular hypoxia (Fig. 2h and i). Compared with a strong fluorescence signal (red) in the control group, there was almost no fluorescence signal in TKM + LED and PTKM NPs + LED-treated groups, suggesting that the TKM and PTKM NPs effectively generate and release oxygen to greatly alleviate hypoxia based on their CAT-like activity and photosynthetic capacity under light irradiation. Moreover, the PTKM NPs promoted HUVECs migration (Fig. S9), which is essential for angiogenesis at the wound sites.

In diabetic wounds, high glucose-induced ROS accumulation triggers mitochondrial dysfunction, which is the main cause of the metabolic disorders that retard wound healing progress [57–61]. To evaluate the mitochondrial dynamics mediated by PTKM NPs in the presence of high-glucose and oxidative environment, HUVECs were simulated by H_2O_2 (50 μM) and glucose (30 mM) for 12 h, followed by the addition of PTKM NPs. MitoTracker Red CMXRos was used as the red fluorescent dye to detect mitochondrial membrane potential (Fig. 2j). The mitochondrial membrane potential (red fluorescence) was reduced in HUVECs cultured under high glucose and H_2O_2 conditions (Fig. S10), indicating an intact mitochondrial membrane potential. In contrast, the mitochondrial membrane potential (red signal) increased in the TKM + LED and PTKM NPs + LED-treated groups. The reversal of the mitochondrial membrane potential was inferred to be due to natural plant-derived PTKM NPs, which could effectively generate oxygen and scavenge ROS to preserve mitochondrial dynamics. Consequently, the HUVECs protected by PTKM NPs survived even under high glucose, high ROS and hypoxia conditions (Fig. 2k).

2.4. PTKM NPs regulate in vitro cellular metabolism

Besides oxygen generation, PTKM NPs can enhance cell metabolism by supplying sufficient ATP and NADPH, which are the fuels necessary for driving the synthesis of substances required for cellular activity [49]. As shown in Fig. 3a and b, intracellular ATP and NADPH concentrations in HUVECs were elevated in the presence of PTKM NPs under LED irradiation (660 nm, 20 W, 1 h), and the production levels increased with increasing PTKM NPs concentrations. However, under dark conditions without LED irradiation, PTKM NPs had no obvious effect on NADPH and ATP levels. This result further confirmed that PTKM NPs could supply exogenous energy (ATP and NADPH) to protect the mitochondria and promote efficient cellular anabolism through the photosynthetic process under LED irradiation (Fig. 3c).

To comprehensively understand the regulatory effect of PTKM NPs on cell metabolism, we compared of the metabolites in HUVECs between the different treatment groups. HUVECs co-incubated with PTKM NPs under high glucose, hypoxic, and high ROS condition were designated as the PTKM NPs-treated group. HUVECs cultured under high glucose conditions were used as positive control. The HUVECs cultured under normal glucose conditions were used as negative control. The hierarchical clustering heatmap showed that the metabolites in HUVECs were significantly different under high glucose, hypoxic, and high ROS culture conditions compared to those under normal culture conditions, and the levels of differential metabolites in the PTKM NPs-treated group were similar to those in the normal group (Fig. S11). Principal component analysis (PCA) of the differential metabolites indicated that the substances detected using the metabolomic method could be clearly distinguished among the three groups (Fig. S12). A Venn diagram shows the relationship between the differential metabolites in each group (Fig. S13), 46 differential metabolites were unique to the comparison group (Control vs Normal vs PTKM). We further screened for differential metabolites between the PTKM and control groups at the threshold of fold-change >1 and p value < 0.05, and identified a total of 2236 metabolites, including 191 upregulated and 194 downregulated (Fig. 3d–f). The differential metabolites between the two groups were mainly amino acids, nucleotides and their derivatives and organic acids and their derivatives. These screened differentially expressed substances were further analyzed using a differential metabolite correlation network. As shown in Fig. 3g and fifty differential metabolites were linked by numerous edges and formed a complex network, indicating that the metabolites in the PTKM NPs-treated cells changed significantly. According to the concept of “clustering factor”, it was observed that L-leucine constituted various edges in the network, revealing that L-leucine played an important central hub role in the correlation network, which may potentially regulate the cell metabolism. Subsequently, the Kyoto Encyclopedia of Genes and Genomes (KEGG) was used to analyze the pathways enriched in the three groups (Fig. S14). The KEGG annotation results showed that metabolism was significantly affected by PTKM NPs. The differential metabolite cluster heatmap of the KEGG pathway also showed evidence that some metabolites in the amino acid and its metabolite pathways (glutathione and L-leucine), and nucleotides and their metabolites were significantly up-regulated in the PTKM group (Fig. 3h). Moreover, the increase production of L-leucine and glutathione was confirmed because violin plots were formed in the PTKM NPs-treated group relative to the control (Fig. 3i and j). By matching the information on differential metabolites according to the

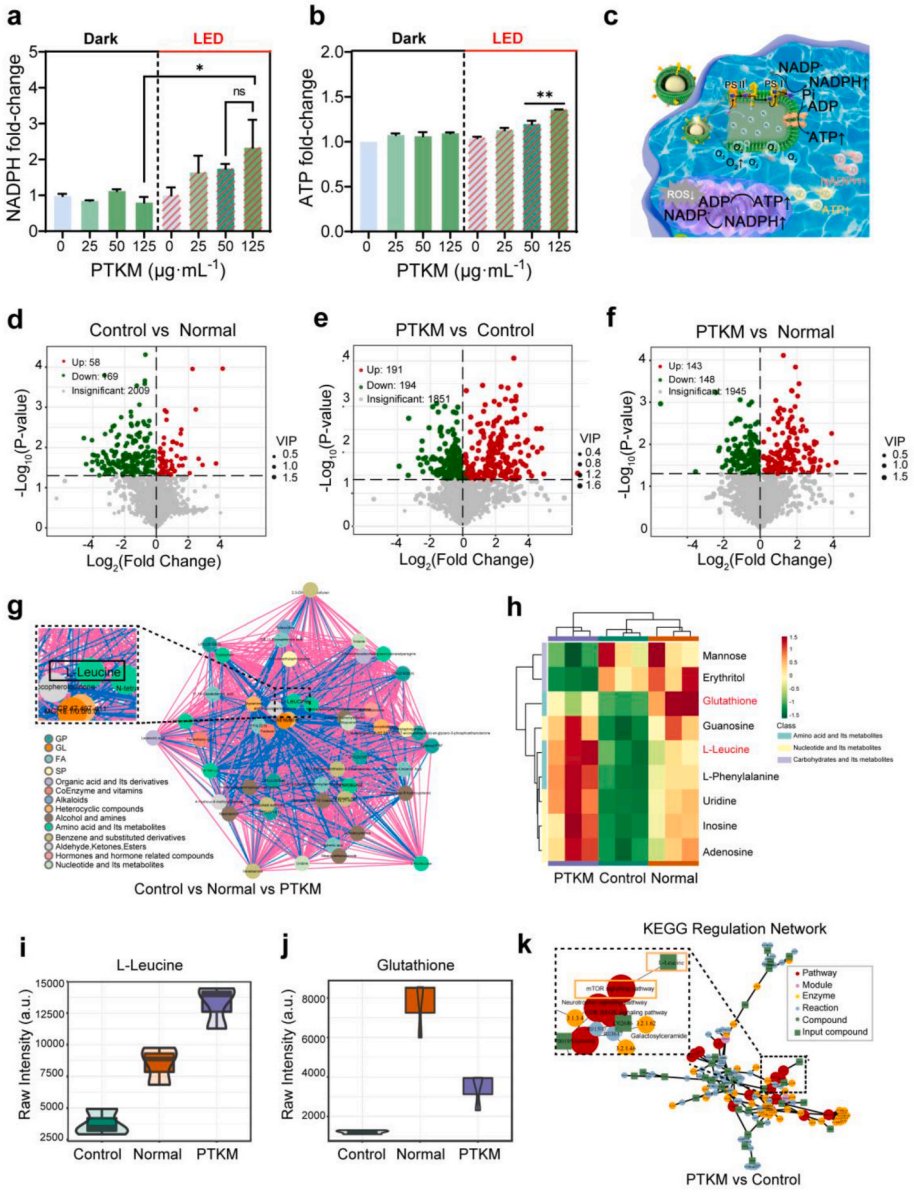

Fig. 3. PTKM NPs promoting cell metabolism. (a) and (b) Intracellular NADPH levels and ATP in HUVECs measured by an NADPH and ATP assay kit, respectively. Cells were co-cultured with PTKM NPs at different concentrations for 6 h and followed by 660 nm-LED irradiation for 1 h. (c) Schematic diagram of the mechanism of PTKM regulates cellular metabolism under 660 nm LED light irradiation. (d), (e) and (f) Volcano plot of differential metabolites in different comparison group. (g) Differential metabolite correlation network diagram in PTKM NPs versus control comparison. (h) Differential metabolite clustering heat map of KEGG pathway, and more than 5 differential metabolites were detected in PTKM NPs versus control versus normal comparison. (i) and (j) The differential metabolite violin plot of L-Leucine and glutathione in the three groups. (k) Diagram of the regulatory network of differential metabolites in PTKM NPs versus control comparison. The selected differential metabolites: VIP>1, *p < 0.05. Normal group: normal cell culturing conditions. Control group: high glucose, hypoxic and high ROS culturing conditions. PTKM NPs group: high glucose, hypoxic and high ROS conditions, co-incubated with PTKM NPs. ns: not significant, *p < 0.05, **p < 0.01. The data are presented as the mean ± s.d. ($n = 3$).

KEGG database, a pathway search and regulatory interaction network analysis showed that L-leucine was directly related to the mTOR signaling pathway (Fig. 3k). L-leucine is the most potent amino acid that activates the mammalian target of rapamycin complex 1 (mTORC1) signaling, which can promote mitochondrial biogenesis and oxidative metabolism to maintain the normal physiological activities of cells [62–64]. Taking together, PTKM NPs can protect the mitochondrial function of HUVECs from high glucose, hypoxic, and high ROS conditions, which is attributed to the following aspects. First, upon light irradiation, PTKM NPs continuously release oxygen, which improves the hypoxic microenvironment and decreases mitochondrial ROS production. Meanwhile, PTKM NPs with polyphenol groups eliminate ROS overproduction. Consequently, the PTKM NPs prevent ROS-induced proton leakage and mitochondrial membrane potential (MMP) alternation [8,65], further preventing functional impairment of the mitochondria. Secondly, PTKM NPs upon light irradiation could supply exogenous energy and mediate the anabolism of intracellular substances, which may eventually trigger the mTOR signaling pathway and lead to mitochondrial biogenesis to enhance mitochondrial function [66, 67].

2.5. PTKM NPs regulating inflammatory response

Macrophages are important inflammatory cells required for wound repair. Macrophage depletion would severely delay re-epithelialization, reduce collagen deposition, impair angiogenesis, and decrease cell

proliferation in the healing [68,69]. Thus, the *anti*-inflammatory ability of PTKM NPs was investigated to inhibit the polarization RAW 264.7 macrophage to M1 phenotype. M1 macrophages activation was induced by the lipopolysaccharide (LPS), followed by co-culture with TKM, PTA and PTKM NPs for 4 h. Macrophage morphology was first assessed microscopically by staining, cells with rhodamine phalloidin (Rhd-phalloidin) to visualize F-actin of the RAW264.7. As shown in Fig. 4a, macrophages in the PTA and PTKM NPs-treated groups maintained round and compact morphology, whereas LPS-induced macrophages were flattened with multiple pseudopodia. This was also demonstrated by the quantification of the RAW264.7 cell area (Fig. 4b). Immunofluorescence staining of CD86 (M1 marker) and CD206 (M2 marker) was further performed to investigate the polarization status of the macrophages. As shown in Fig. 4c and d, both the PTA and PTKM NPs-treated groups exhibited the lowest level of $CD86^+$ signal. While the number of CD206-labeled M2 macrophages was higher in the PTKM NPs-treated group than in the control group (Fig. 4e). Quantitative data showed that the percentage of CD206-labeled M2 macrophages in the PTKM NPs group was higher than that in the blank group (Fig. 4f). These results suggest that PTKM NPs can inhibit M1 polarization and induce M2 polarization, whereas PTA NPs can only inhibit M1 polarization. It was also noted that the reprogramming of pro-inflammatory M1 macrophages into anti-inflammatory M2 macrophages by PTKM NPs was independent of LED exposure. Flow cytometry data further confirmed the fluorescence trends (Fig. 4g). In the groups treated with PTKM NPs + LED, the expression of the M2 macrophage molecular marker (CD206) significantly increased, whereas the expression of the M1 macrophage molecular marker (CD86) decreased. The supply of O_2 from the photosynthesis of PTKM NPs can prevent the M1 phenotype switching of macrophages and prevent them from overexpressing hypoxia-inducible factor-1α (HIF-1α), thereby promoting the reprogramming of macrophages to a proregenerative M2 phenotype [70]. Thus, PTKM NPs exert anti-inflammatory effects by suppressing M1 macrophage polarization and promoting M2 macrophage activation, which is favorable for chronic diabetic wound repair.

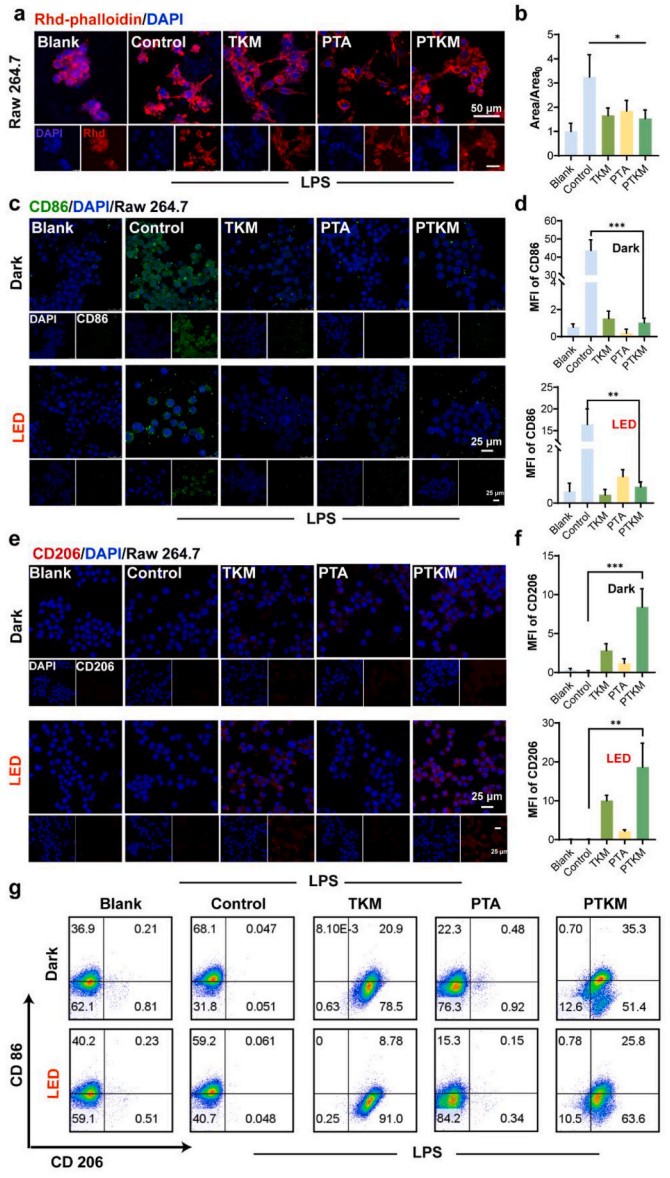

Fig. 4. In vitro evaluating immune modulation of PTKM NPs. (a) Fluorescence microscopic images and (b) quantification of cytoskeleton-stained RAW 264.7 cells treated by LPS and co-cultured with different nanoparticles for 4 h. (c) Immunofluorescence staining and (d) quantification of CD86 in RAW 264.7 cells following 12 h of inflammatory stimulation. (e) Immunofluorescence staining and (f) quantification of CD206 in RAW 264.7 cells following 12 h of inflammatory stimulation. (g) Representative flow cytometry plots showing the presence of $CD86^+$ M1 macrophages and $CD206^+$ M2 macrophages after 12 h of inflammatory stimulation. *$p < 0.05$, **$p < 0.01$. The data are presented as the mean ± s.d. ($n = 3$).

2.6. Fabrication and characterizations of PTKM-incorporated hydrogels

To effectively deliver and retain PTKM NPs at the wound sites, a pH-responsive adhesive hydrogel composed of hyaluronic acid (HA) and gelatin (Gel) was employed to incorporate PTKM NPs [71,72]. Prior to hydrogel fabrication, gelatin was modified with ethylenediamine to form amino-modified gelatin ($Gel\text{-}NH_2$) with more amino groups [73,74], whereas hyaluronic acid was oxidized to form OHA containing reactive aldehyde groups. Then the hydrogel was then synthesized formed based on the Schiff base reaction between $Gel\text{-}NH_2$ and OHA to obtain a stable crosslinked matrix. FTIR techniques and ^{1}hydrogen-nuclear magnetic resonance (^{1}H NMR) spectrometry confirmed the successful synthesis of OHA, $Gel\text{-}NH_2$, and HG hydrogels (Figs. S15 and S16). Subsequently, 3 wt % of PTKM NPs was incorporated into the HG matrix to fabricate the PTKM@HG hydrogel. The microscopic morphology of the freeze-dried PTKM@HG hydrogel was observed by scanning electron microscope (SEM), which showed that the hydrogel exhibited a highly porous and interconnected network (Fig. S17). The higher magnification SEM image indicated that the PTKM NPs were scattered on the interior of the PTKM@HG hydrogel (Fig. 5a). Moreover, CLSM 3D micrographs of the FITC-labeled PTKM@HG hydrogel indicated that the PTKM NPs were uniformly dispersed in the HG hydrogel (Fig. 5b). The mechanical behavior of the PTKM@HG hydrogel with 3 wt % PTKM NPs were evaluated with the rheological tests. The strain amplitude sweep test showed that both the G′ and G″ modulus and loss modulus exhibited a sharp decrease at a yield strain of ~200 % (Fig. 5c). The frequency sweep revealed that the PTKM@HG hydrogel exhibited viscoelastic properties with a storage modulus (G′) of 1 kPa (Fig. 5d), which is lower than the modulus of human skin tissues [75]. Owing to the dynamic nature of the Schiff-base covalent bonds in the hydrogel, the PTKM@HG hydrogel displayed an excellent self-healing ability. As shown in Fig. 5e, the hydrogel was cut into two pieces from separate hydrogels labeled with rhodamine B and methylene blue, and then the two hydrogel pieces healed into a single piece after 10 min of physical contact. A step-strain sweep was performed to further evaluate the self-healing ability of the PTKM@HG hydrogel. The continuous shear strain was alternated between 500 % and 0.1 % at a fixed angular frequency of 5 rad/s, respectively. When the PTKM@HG hydrogel was subjected to a higher strain of 500 %, the PTKM@HG hydrogel was broken with larger G'' than G' (Fig. 5f). Subsequently, when the PTKM@HG hydrogel was applied with a lower strain of 0.01 %, the G' and G''values were instantaneously fully restored to their original

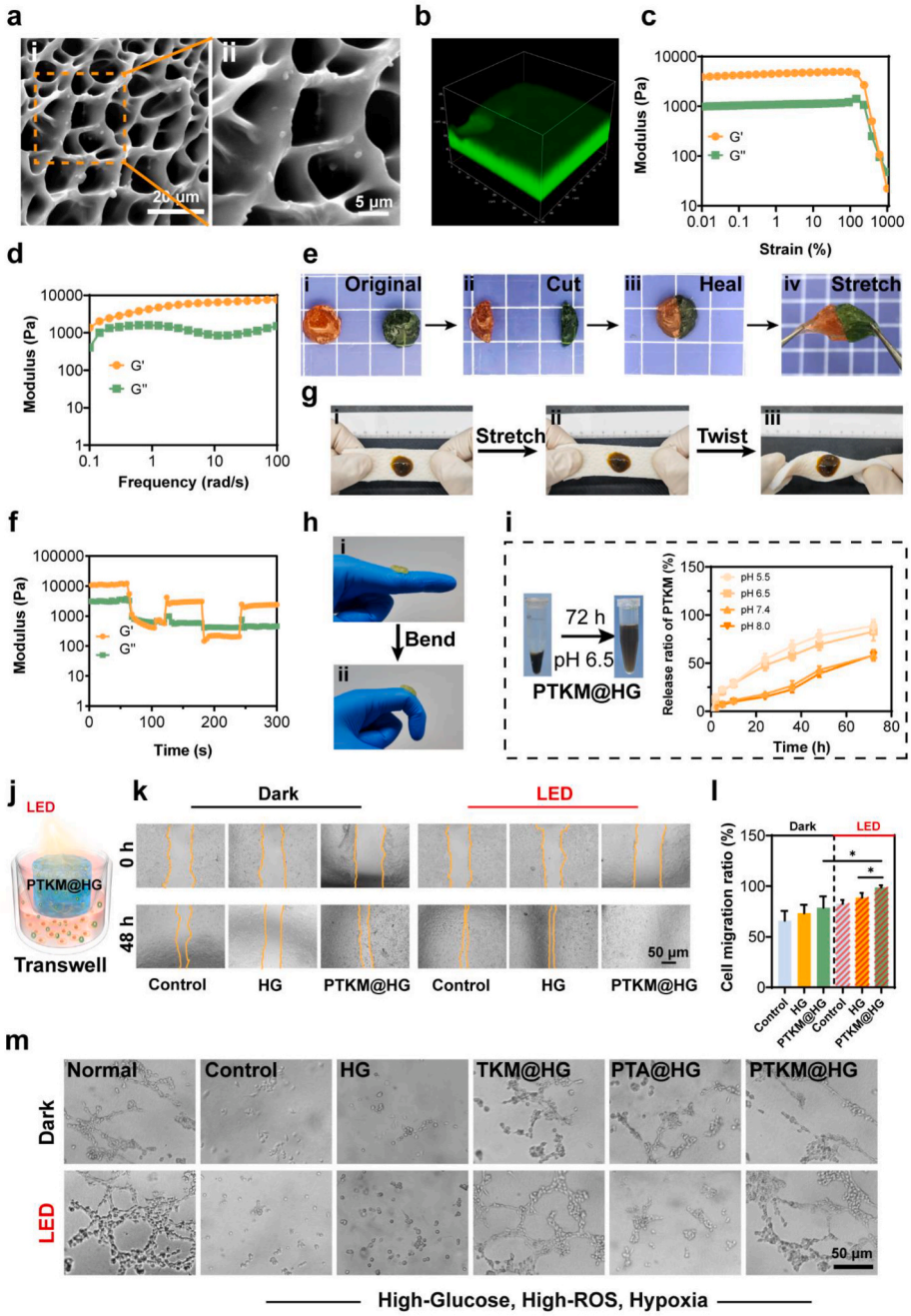

Fig. 5. Characterizations of the PTKM@HG hydrogel. (a) SEM images of PTKM@HG hydrogel. (b) CLSM image showing the uniform distribution of FITC-labeled PTKM NPs in the hydrogel. (c) and (d) Rheological property of PTKM@HG hydrogel. (e) Macroscopic self-healing ability of PTKM@HG hydrogels. Rhodamine B and methylene blue were incorporated into the hydrogels for visualization. (f) Strain measurement of PTKM@HG hydrogel. (g) Adhesion capacity of PTKM@HG hydrogel on porcine skin under stretching, bending, or twisting. (h) Photographs showing the hydrogel adhesion to finger joints. (i) Release curves of PTKM NPs from the hydrogel in various buffers (pH 5.5, 6.5, 7.4, and 8.0). (j) Schematic illustration of a transwell system to evaluate the HaCaTs migration with PTKM@HG with LED irradiation. (k) Representative phase-contrast images of HaCaTs migration under HG and PTK@HG hydrogels treatment at time intervals of 0 and 48 h without or with LED irradiation. The time for LED irradiation was 30 min per 12 h. (l) Quantification of cell-covered area after 48 h of culturing. (m) Representation images of HUVECs tube formation for 6 h of treatment by different hydrogels. Scale bar: 50 μm. ns: not significant, *p < 0.05. The data are presented as the mean ± s.d. ($n = 3$).

values even after repeated multiple times. These results indicated the self-healing behavior of the PTKM@HG hydrogel. In addition, the PTKM@HG hydrogel showed strong adhesion to the porcine skin without detachment after stretching and twisting (Fig. 5g), and was sufficiently flexible to deform with curved finger joints (Fig. 5h). In addition, the adhesive strength of the PTKM@HG hydrogel was measured via a lap-shear test using a universal mechanical testing machine, and fresh porcine skin was used as a typical soft biological sample. The adhesive strength of the PTKM@HG hydrogel to porcine skin was as high as 32.73 kPa (Fig. S18). These results suggest that the PTKM@HG hydrogel with soft, self-healing, tissue-adhesive, and flexible properties has great potential as wound dressing.

To assess the delivery efficiency of the PTKM NPs from the hydrogels, the PTKM@HG hydrogel was immersed in various buffers with different pH values (5.5, 6.5, 7.4, 8.0) and the release profile of PTKM from the hydrogels were investigated. As shown in Fig. 5i, nearly 90 % of PTKM NPs was released from the hydrogel in 72 h under simulated acidic environments (pH 5.5 and 6.5), which was due to the hydrolysis of the

Schiff base linkages under acidic condition, allowing the efficient release of PTKM NPs from the loose hydrogel. To further recapitulate the topical application of PTKM@HG hydrogel at wound sites, the effect of released PTKM NPs from hydrogels on human immortalized keratinocytes (HaCaTs) was evaluated in a transwell system with or without LED irradiation. Live/dead staining demonstrated that the PTKM@HG hydrogel did not affect on cell viability (Fig. S19). Moreover, the in vitro scratch assays revealed that the PTKM@HG hydrogel accelerated the HaCaTs migration upon LED irradiation (Fig. 5j). As shown in Fig. 5k and l, after 48 h of incubation, the migration rate of HaCaTs was significantly higher in the PTKM@HG + LED groups than in the control groups and PTKM@HG groups without LED irradiation. Second, the angiogenic capability of HUVECs seeded on different hydrogels (HG, TKM@HG, PTA@HG and PTKM@HG) was evaluated using a Matrigel small tube formation assay under high glucose, hypoxic, and high ROS culture conditions. The tube length and branches of the HUVECs were severely limited under the high glucose, hypoxic, and high ROS conditions (Fig. 5m). In contrast, HUVECs seeded on the PTKM@HG hydrogel upon LED irradiation exhibited increased branch points and tube length, indicating that the PTKM@HG hydrogel can effectively promote angiogenesis even under high glucose, hypoxic, and high ROS conditions. These results confirmed the enhanced angiogenesis was attributed

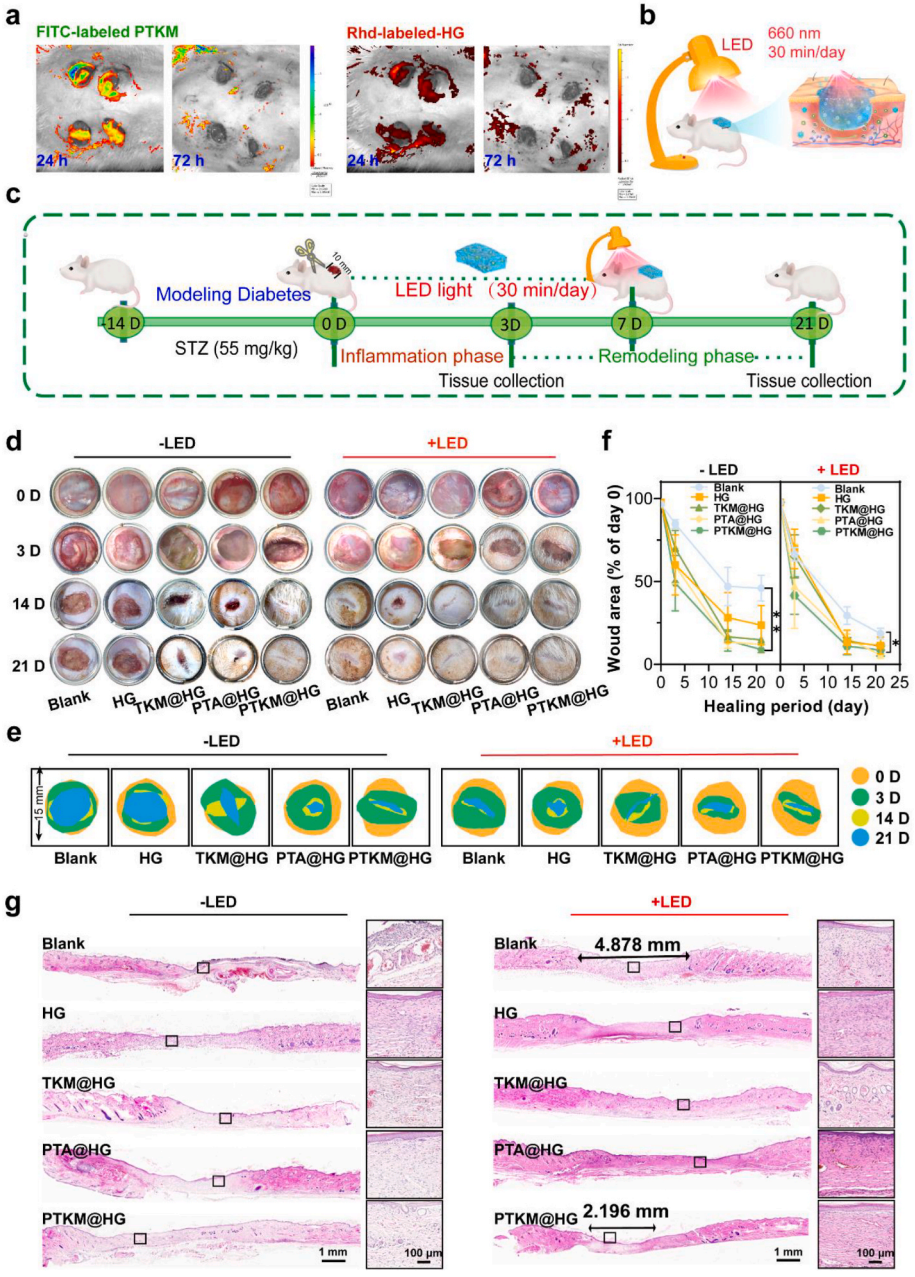

Fig. 6. Therapeutic effect of PTKM@HG hydrogel on diabetic wounds repairing without or with LED irradiation. (a) In vivo fluorescent imaging of the PTKM@HG hydrogel at different time points. PTKM NPs were labeled by FITC, and the HG hydrogel was labeled by Rhodamine B (Rhd). (b) Schematic diagram of design of animal experiments to test the therapeutic effect of PTKM@HG hydrogel in diabetic rat model under LED irradiation. (c) Schematic illustration of animal therapy by PTKM@HG hydrogel. (d) Representative images of the wounds in different treatment groups with or without 660 nm LED irradiation for day 21. The time for LED irradiation was 30 min per day for 7 days. (e) The area traces of mice wound healing in various treatment groups on days 0, 3, 7, 14, and 21. (f) Wound size changes during 21 days of post healing. Wound size at each time point was normalized to day 0. (g) Representative hematoxylin and eosin staining images of wound tissues treated with different groups on day 21. *$p < 0.05$. The data are presented as the mean ± s.d. ($n = 3$).

to ROS scavenging, soluble oxygen production, and energy supply by the PTKM@HG hydrogel, which was in consistent with previous studies [11,73,76]. These results indicate that the PTKM@HG hydrogel has good cytocompatibility and can effectively release PTKM NPs to promote cell proliferation, migration, and angiogenesis upon LED irradiation, which is critical for the regeneration of the epidermis and dermis to accelerate wound closure.

2.7. In vivo promoting diabetic chronic wound healing

Prior to investigating the in vivo therapeutic efficacy of the hydrogel, the decomposition and skin penetration of the PTKM@HG hydrogel were investigated in vivo because of its significant roles in skin-related applications. To visualize the penetration process, PTKM NPs were labeled with FITC (green), and HG hydrogel were labeled with rhodamine B (red). Fluorescence images of the PTKM@HG hydrogel at wound sites were acquired using an in-vivo fluorescence imaging system. High fluorescence intensities of both PTKM NPs and HG hydrogel were observed at 24 and 72 h after implantation (Fig. 6a). In addition, green fluorescence was observed at the epidermis region and colonized skin epidermis, indicating that the PTKM NPs was able to penetrate through stratum corneum.

Next, the regenerative capacity of the PTKM@HG hydrogel was explored in vivo by administering the hydrogel to full-thickness wounds (10 mm in diameter) of diabetic rats. Subsequent treatments consisting of normal saline (blank group), HG, TKM@HG, PTA@HG, and PTKM@HG hydrogels with or without LED irradiation were assessed by continuous observation and tissue collection on day 21. The duration of LED irradiation (660 nm, 20 W) of the wound site was 30 min per day (Fig. 6b). The wound healing process was monitored on day 21 (Fig. 6c). Representative images of the wounds showed that blank diabetic wounds without any treatment were difficult to heal completely even after day 21 (Fig. 6d). The hydrogels (TKM@HG, PTA@HG and PTKM@HG) treated groups induced faster-wound healing than the blank group. Additionally, LED irradiation was beneficial for wound healing. Compared with the groups without LED irradiation which still had distinct wounds, all LED-irradiated groups showed decreased wound size (Fig. 6e). The quantification results showed that the PTKM@HG hydrogel + LED treatment attained the best healing effect with a wound closure ratio of 91.4 % on day 21 (Fig. 6f). Hematoxylin-eosin (H&E) staining was performed to investigate the histological changes in the wounds of the different treatment groups. On day 21, the blank group still showed large scabs and irregular skin structure, which was infiltrated by inflammatory cells. In the PTKM@HG hydrogel + LED-treated wounds, the epidermis and dermis of the skin were relatively intact and highly ordered with low infiltration of inflammatory cells (Fig. 6g). In addition, H&E staining of the sections showed that the granulation tissue gap in the PTKM@HG hydrogel + LED group was the smallest among all the groups, indicating that the TKM@HG hydrogel accelerated the proliferative phase of chronic wounds under 660 nm-LED irradiation.

2.8. Antioxidative and immunomodulatory ability of the PTKM@HG hydrogel in vivo

A more comprehensive study was conducted to analyze the underlying mechanism of the PTKM@HG hydrogel that in the regulation of the wound healing process. H&E staining was performed to investigate the infiltration of inflammatory cells into the wound sites of the different treatment groups. Tissue sections from the untreated control group showed significant infiltration of inflammatory cells. By contrast, almost no inflammatory cell infiltration was observed in the PTKM@HG-treated group under LED irradiation (Fig. S20). Moreover, the antioxidative effect of the hydrogels in protecting cellular components such as lipids and DNA from oxidative stress damage was investigated using immunofluorescence staining for 4-hydroxy-2-nonenal (4-HNE) and 8-hydroxydeoxyguanosine (8-OHdG) on day 3. As shown in Fig. 7a-d, the lowest 4-HNE and 8-OHdG levels were observed in the PTKM@HG + LED group among all the groups, indicating that the PTKM@HG hydrogel relieved oxidative stress at the initial stage of the diabetic wound healing process. Next, the anti-inflammatory ability of the hydrogels was investigated by examining the infiltration and polarization of macrophages at the wound sites on day 3 (Fig. S21). As shown in Fig. 7e–f, immunofluorescent staining of the CD86 marker showed a large number of M1 macrophages (green fluorescence) in the blank and HG groups, suggesting a severe inflammatory response. In contrast, the PTKM@HG hydrogel-treated group showed decreased expression of CD86-positive M1 macrophages and increased expression of CD206-positive M2 macrophages (red fluorescence), compared to the blank and HG hydrogel-treated groups (Fig. 7g). Quantitative measurements verified that the PTKM@HG hydrogel significantly alleviated inflammation and enhanced the infiltration and distribution of M2 macrophages at the wound sites (Fig. 7h). The results of the in vitro and in vivo experiments confirmed that the PTKM@HG hydrogel effectively decreased M1 macrophage activation and induced the polarization of the M2 phenotype, which was beneficial for the formation of a regenerative microenvironment for diabetic wound healing [69].

2.9. Oxygen and energy supplying ability of the PTKM@HG hydrogel to promote neovascularization and re-epithelization in diabetic wounds

The oxygen supply ability of the PTKM@HG hydrogel at the wound sites was further examined by immunofluorescence staining of hypoxia-inducible factor-1α (HIF-1α). The immunofluorescence intensity of HIF-1α was the lowest in the PTKM@HG + LED group among all the groups, confirming that the PTKM@HG hydrogel could release oxygen to ameliorate local hypoxia at the wound site upon LED irradiation (Fig. 7i and j). In conclusion, PTKM@HG significantly reduced oxidative stress at the wound site, promote macrophage polarization, regulate the M1/M2 ratio, alleviate local hypoxia and provided a suitable microenvironment for wound healing in the early stages of wound healing (inflammatory stage) (Fig. 7k).

The cellular metabolism at the wound sites was then examined by immunofluorescence staining of peroxisome proliferator activated receptor γ coactivator-1α (PGC-1α) on both day 3 and day 21 (Fig. 8a–d). Compared with the blank group, the PTKM@HG hydrogel + LED treatment significantly increased the density of PGC-1α$^+$ cells at both time points, indicating that the PTKM@HG hydrogel with oxygen generation and ROS scavenging activity could protect mitochondrial function and enhance cell metabolism in both early and late stages of wound healing process. The reconstruction of neovascularization is crucial in delivering nutrients and oxygen to metabolically demanding wounds, thereby facilitating the formation of granulation tissue, which was evaluated by immunofluorescence staining of endothelial-specific markers (CD31) and α-smooth muscle actin (α-SMA) of tissue sections (Fig. S22). As shown in Fig. 8e–h, the PTKM@HG hydrogel + LED treatment enhanced the regeneration of new blood vessels in the wound area, facilitating the transportation of oxygen and nutrition to the wound sites, which is essential for wound repair.

In the later period of healing, re-epithelization is another important event in skin repairing mechanism. The primary epidermal markers such as the basal keratin marker (CK14) and keratin marker (CK10) were assessed by immunofluorescence staining of the wound tissues on day 21. In the PTKM@HG + LED treated groups, the wound gap was almost closed and covered by a mature and spinous layer composed of CK10$^+$ keratinocytes, whereas the keratinocyte migration was much slower in the blank group (Fig. 8i and j). In addition, the immunofluorescence staining of CK14 revealed a significantly increased hair follicle density in PTKM@HG + LED treated wounds in the epidermal basal layer (Fig. 8k, l and 8m). These results demonstrated that the PTKM@HG hydrogel could effectively promote re-epithelialization by inducing keratinocyte migration and hair follicle formation. Collectively, these

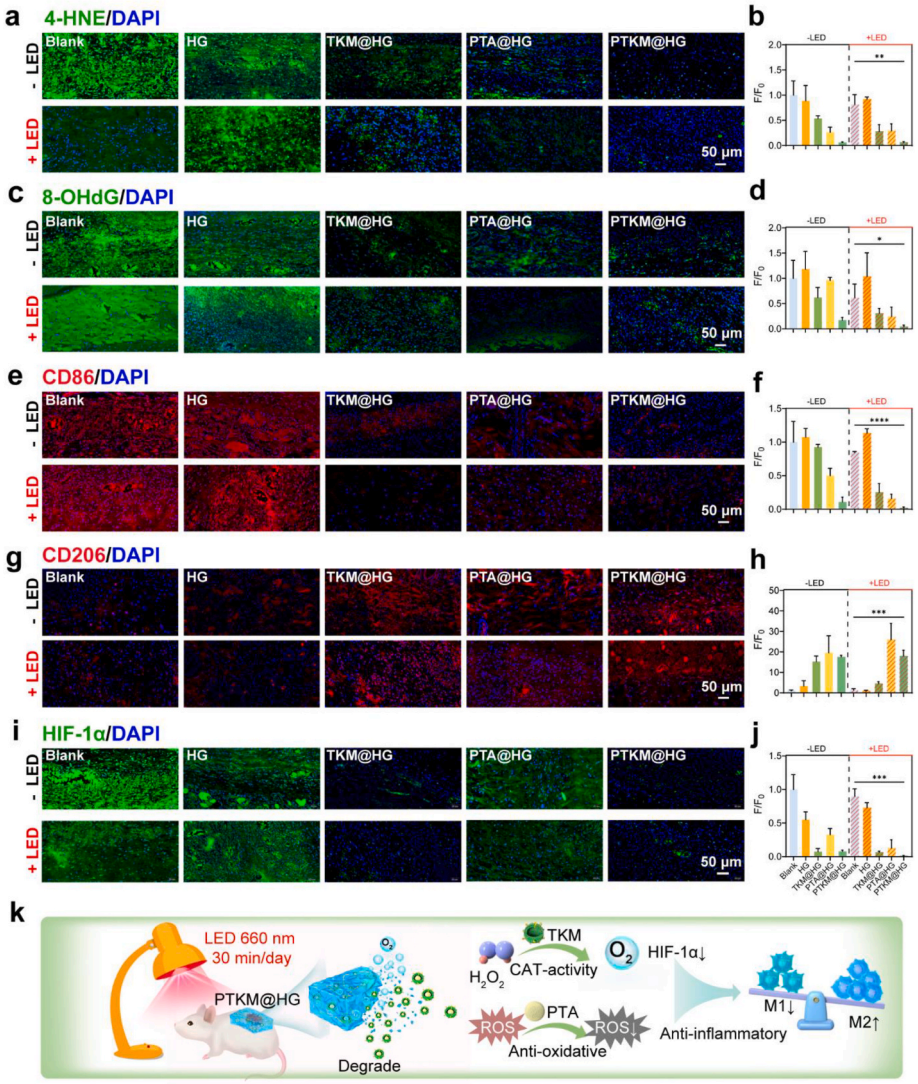

Fig. 7. In vivo immune modulation of PTKM@HG hydrogel at wound sites on day 3. Immunofluorescence staining of (a) 4-HNE (lipid peroxidation marker) and (c) 8-OHdG (DNA damage marker) in the wound tissues. Immunofluorescence staining of (e) CD86 (M1 macrophages marker) and (g) CD206 (M2 macrophages marker) in the wound tissues. (i) Immunofluorescence staining of HIF-1α (hypoxia marker) in the wound tissues. (b), (d), (f), (h) and (j) Fluorescent quantitation (F/F_0) of tissue sections of wound area for 4-HNE, 8-OHdG, CD86, CD206, and HIF-1α, respectively. Cell nuclei were stained with DAPI in all immunofluorescence staining images. (k) Schematic illustration of the PTKM@HG hydrogel for regulating diabetic wound microenvironments during the early healing period in the following three aspects, including (1) releasing PTKM NPs into the wound microenvironment (2) supplying oxygen to alleviate hypoxia and (3) reducing inflammation and oxidative stress. The data are presented as the mean ± s.d. ($n = 3$).

findings provide evidence that the incorporation of photosynthetic PTKM NPs into the hydrogel as a therapeutic oxygen delivery and metabolism regulation system upon light irradiation, can alleviate oxidative stress, reduce inflammation, and promote neovascularization of re-epithelization, which is a promising approach to accelerate the wound healing process in individuals suffering from chronic diabetes.

3. Conclusion

The treatment of diabetic wounds is a very complex due to the impaired mitochondrial function caused by oxidative stress, hypoxia and inflammatory microenvironments. Therefore, the exploring a comprehensive strategy that can protect mitochondria and correct metabolic disorders will fundamentally accelerate the healing process of chronic wounds. The nature-derived thylakoid membranes from plant leaves display excellent oxygenation and generation of metabolites facilitated by the photosynthetic process, which holds great potential for treating diabetic wounds (Table S1) [77]. However, strategies based on thylakoid-based photosynthetic nanoarchitectures have not been intensively investigated, limiting their biomedical applications.

In this study, we developed artificial photosynthetic nanoparticles (PTKM NPs) by coating polyphenol nanoparticles with thylakoid membranes, and incorporating the PTKM NPs into a biopolymer-based biodegradable hydrogel (PTKM@HG hydrogel) to form light-driven bioenergetic and oxygen-releasing hydrogel. The obtained PTKM NPs exhibited a prominent photosynthetic effect releasing oxygen and producing exogenous ATP and NADPH when exposed to natural or mild red light, thereby overcoming the inevitable skin damage caused by conventional laser-induced phototherapy. Notably, the continuous oxygen release could effectively improve the hypoxic microenvironment, reduce the expression of HIF-1α, and protect mitochondria from oxidative stress. The exogenous energy and oxygen supplied by PTKM NPs regulate amino acid metabolism, which may eventually trigger the mTOR signaling pathway and substantially lead to mitochondrial biogenesis to enhance the mitochondrial function of cells in high glucose, hypoxic, and high ROS environments in diabetic wounds. Moreover, PTKM NPs

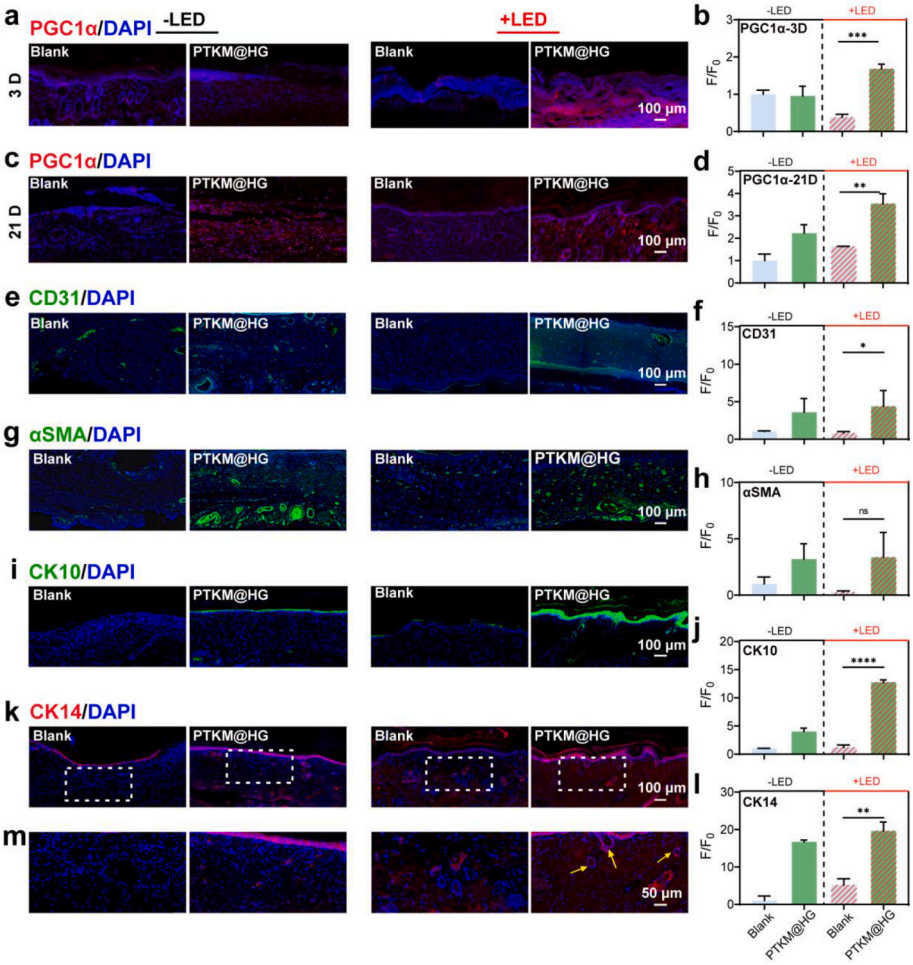

Fig. 8. PTKM@HG hydrogel accelerating wound healing in diabetic rats. (a) and (c) Immunofluorescence staining of PGC-1α (red) on day 3 and day 21. (e) Immunofluorescence staining of CD31 (green), (g) α-SMA (green), (i) cytokeratin 10 (CK10, green) and (k) cytokeratin 14 (CK14, red) at the wounded regions. (m) Enlarged images of the white box in (k), yellow arrows indicate hair follicle. Cell nuclei were stained with DAPI (blue). (b), (d), (f), (h), (j) and (l) Relative quantitative analysis. ns is no significant difference, *P < 0.05, **P < 0.01, ***P < 0.001, ****P < 0.0001. The data are presented as the mean ± s.d. ($n = 3$).

mitigate excessive ROS production in a high glucose microenvironment and induce M2-macrophage polarization. Consequently, the PTKM@HG hydrogel promoted the diabetic wound repair in a comprehensive manner, including the effective release of PTKM NPs to correct the hyperglycemia-induced microenvironment characterized by persistent inflammation, elevated ROS levels, and disordered metabolism, and expedited the regeneration of the epidermis and dermis upon red-light irradiation.

In summary, The PTKM@HG hydrogel present certain advantages significant for clinical applications. First, the matrix of PTKM@HG hydrogel is based on biodegradable hyaluronic acid and gelatin and the PTKM NPs composed of plant-derived thylakoid membranes and polyphenols, which show excellent biocompatibility, improved cellular activity, and weak immune response in clinical applications over synthetic polymers [8,42,78–82]. Second, the red LED light, as a cold and mild light source, instead of the laser was used to drive photosynthesis of the PTKM@HG hydrogel to generate oxygen and supply energy for wound healing, which avoids the risk of laser-caused damage to the stratum corneum and melanin precipitation, while the red LED light also plays a positive effect on promoting the repair of damaged skin [83] and inhibiting inflammation [84] for clinical applications. Together, this work not only provides an efficient strategy for diabetic wound healing but also for other degenerative diseases by delivering key metabolites and energy to achieve effective therapy through such hydrogels.

Data availability

Data will be made available on request.

Ethics approval and consent to participate

All the animal experiments were approved by School of Medicine and Pharmacy, Ocean University of China Animal Laboratory Animal Ethics Committee (Approval Number: OUC-SMP-2023-03-07). All the authors were in compliance with all relevant ethical regulations.

CRediT authorship contribution statement

Yuping Jiang: Writing – original draft, Software, Methodology, Investigation, Formal analysis, Data curation, Conceptualization. **Xiaomin Feng:** Formal analysis, Data curation. **Xin Qiao:** Software, Data curation. **Yufeng Li:** Formal analysis. **Xiaozhuang Li:** Formal analysis. **Jinguang Yang:** Writing – review & editing. **Lu Han:** Writing – review & editing, Writing – original draft, Supervision, Project administration, Funding acquisition, Conceptualization.

Declaration of competing interest

We declare that we have no financial and personal relationships with other people or organizations that can inappropriately influence this

manuscript titled “Plant-inspired visible-light-driven bioenergetic hydrogels for chronic wound healing”. There is no professional or other personal interest of any nature or kind in any product, service and/or company that could be construed as influencing the position presented in, or the review of, the manuscript entitled.

Acknowledgements

This work was supported by Fundamental Research Funds for Central Universities (202241010), Natural Science Fund for Excellent Young Scholars of Shandong Province (ZR202110120029), the Major science and technology projects (110202201020 (LS-04)), and Open Project of the Key Laboratory for Tobacco Disease and Pest Monitoring and Comprehensive Management in the Tobacco Industry (KLTPMIMT2022-11).

Appendix A. Supplementary data

Supplementary data to this article can be found online at https://doi.org/10.1016/j.bioactmat.2024.08.003.

References

[1] H. Xia, Z. Dong, Q. Tang, R. Ding, Y. Bai, K. Zhou, L. Wu, L. Hao, Y. He, J. Yang, H. Mao, Z. Gu, Glycopeptide-based multifunctional hydrogels promote diabetic wound healing through pH regulation of microenvironment, Adv. Funct. Mater. 33 (2023) 2215116.
[2] W. Liu, X. Zhai, X. Zhao, Y. Cai, X. Zhang, K. Xu, J. Weng, J. Li, X. Chen, Multifunctional double-layer and dual drug-loaded microneedle patch promotes diabetic wound healing, Adv. Healthcare Mater. 12 (2023) 2300297.
[3] N. Shao, S. Huang, Y. Huang, M. Pan, Y. Xie, Q. Chen, C. Chen, J. Pan, Y. Zhou, Smart enzyme-like polyphenol-copper spray for enhanced bacteria-infected diabetic wound healing, Small 20 (2023) 2308295.
[4] S. Shen, L. Shi, D. Fan, C. Zhu, M. Jiang, Y. Dong, Ginsenoside Rg5 nanomedicine composited hydrogel with metabolic regulation and immunomodulation properties for tunneling diabetic wounds therapy, Chem. Eng. J. 469 (2023) 143989.
[5] M. Roden, G.I. Shulman, The integrative biology of type 2 diabetes, Nature 576 (2019) 51–60.
[6] J. Liu, M. Qu, C. Wang, Y. Xue, H. Huang, Q. Chen, W. Sun, X. Zhou, G. Xu, X. Jiang, A dual-cross-linked hydrogel patch for promoting diabetic wound healing, Small 18 (2022) 2106172.
[7] K. Sada, T. Nishikawa, D. Kukidome, T. Yoshinaga, N. Kajihara, K. Sonoda, T. Senokuchi, H. Motoshima, T. Matsumura, E. Araki, Hyperglycemia induces cellular hypoxia through production of mitochondrial ROS followed by suppression of aquaporin-1, PLoS One 11 (2016) e0158619.
[8] Y. Guan, H. Niu, Z. Liu, Y. Dang, J. Shen, M. Zayed, L. Ma, J. Guan, Sustained oxygenation accelerates diabetic wound healing by promoting epithelialization and angiogenesis and decreasing inflammation, Sci. Adv. 7 (2021) eabj0153.
[9] H. Du, B. Li, R. Yu, X. Lu, C. Li, H. Zhang, F. Yang, R. Zhao, W. Bao, X. Yin, Y. Wang, J. Zhou, J. Xu, ETV2 regulating PHD2-HIF-1α axis controls metabolism reprogramming promotes vascularized bone regeneration, Bioact. Mater. 37 (2024) 222–238.
[10] H.-H. Chen, F.-S. Fu, Q.-W. Chen, Y. Zhang, X.-Z. Zhang, Two-pronged microbe delivery of nitric oxide and oxygen for diabetic wound healing, Nano Lett. 23 (2023) 5595–5602.
[11] Y. Li, R. Fu, Z. Duan, C. Zhu, D. Fan, Artificial nonenzymatic antioxidant MXene nanosheet-anchored injectable hydrogel as a mild photothermal-controlled oxygen release platform for diabetic wound healing, ACS Nano 16 (2022) 7486–7502.
[12] C. Bursill, K.R. Primer, E. Solly, P.J. Psaltis, J.T.M. Tan, P731High-density lipoproteins rescue diabetes-impaired angiogenesis by restoring cellular metabolic reprogramming responses to hypoxia, Eur. Heart J. 40 (2019) ehz747.0335.
[13] J.-N. Wang, Q. Yang, C. Yang, Y.-T. Cai, T. Xing, L. Gao, F. Wang, X. Chen, X.-Q. Liu, X.-Y. He, B. Wei, L. Jiang, C. Li, J. Jin, J.-G. Wen, T.-T. Ma, H.-Y. Chen, J. Li, X.-M. Meng, Smad 3 promotes AKI sensitivity in diabetic mice via interaction with p53 and induction of NOX4-dependent ROS production, Redox Biol. 32 (2020) 101479.
[14] F.R. Palma, B.N. Gantner, M.J. Sakiyama, C. Kayzuka, S. Shukla, R. Lacchini, B. Cunniff, M.G. Bonini, ROS production by mitochondria: function or dysfunction? Oncogene 43 (2024) 295–303.
[15] M. Giacomello, A. Pyakurel, C. Glytsou, L. Scorrano, The cell biology of mitochondrial membrane dynamics, Nat. Rev. Mol. Cell Biol. 21 (2020) 204–224.
[16] A.S. Monzel, J.A. Enríquez, M. Picard, Multifaceted mitochondria: moving mitochondrial science beyond function and dysfunction, Nat. Metab. 5 (2023) 546–562.
[17] V. Sorrentino, K.J. Menzies, J. Auwerx, Repairing mitochondrial dysfunction in disease, Annu. Rev. Pharmacol. Toxicol. 58 (2018) 353–389.
[18] Q.-S. Deng, Y. Gao, B.-Y. Rui, X.-R. Li, P.-L. Liu, Z.-Y. Han, Z.-Y. Wei, C.-R. Zhang, F. Wang, H. Dawes, T.-H. Zhu, S.-C. Tao, S.-C. Guo, Double-network hydrogel enhanced by SS31-loaded mesoporous polydopamine nanoparticles: symphonic collaboration of near-infrared photothermal antibacterial effect and mitochondrial maintenance for full-thickness wound healing in diabetes mellitus, Bioact. Mater. 27 (2023) 409–428.
[19] A. El-Kenawi, B. Ruffell, Inflammation, ROS, and mutagenesis, Cancer Cell 32 (2017) 727–729.
[20] C. Shi, J. Dawulieti, F. Shi, C. Yang, Q. Qin, T. Shi, L. Wang, H. Hu, M. Sun, L. Ren, F. Chen, Y. Zhao, F. Liu, M. Li, L. Mu, D. Liu, D. Shao, K.W. Leong, J. She, A nanoparticulate dual scavenger for targeted therapy of inflammatory bowel disease, Sci. Adv. 8 (2022) eabj2372.
[21] L. He, G. Huang, H. Liu, C. Sang, X. Liu, T. Chen, Highly bioactive zeolitic imidazolate framework-8–capped nanotherapeutics for efficient reversal of reperfusion-induced injury in ischemic stroke, Sci. Adv. 6 (2020) eaay9751.
[22] H. Wei, H. Huang, H. He, Y. Xiao, L. Chun, Z. Jin, H. Li, L. Zheng, J. Zhao, Z. Qin, Pt–Se hybrid nanozymes with potent catalytic activities to scavenge ROS/RONS and regulate macrophage polarization for osteoarthritis therapy, Research 7 (2024) 310.
[23] T.A. Wynn, A. Chawla, J.W. Pollard, Macrophage biology in development, homeostasis and disease, Nature 496 (2013) 445–455.
[24] A. Shapouri-Moghaddam, S. Mohammadian, H. Vazini, M. Taghadosi, S.-A. Esmaeili, F. Mardani, B. Seifi, A. Mohammadi, J.T. Afshari, A. Sahebkar, Macrophage plasticity, polarization, and function in health and disease, J. Cell. Physiol. 233 (2018) 6425–6440.
[25] C. Liu, Y. Wang, P. Wang, Y. Gong, B. Yi, J. Ruan, X. Wang, In situ electrospun aloe-nanofiber membrane for chronic wound healing, Smart Mater. Med. 4 (2023) 514–521.
[26] R. Dong, M. Chen, Y. Jia, H. Tang, Z. Xiong, Y. Long, X. Jiang, An in situ dressing material containing a multi-armed antibiotic for healing irregular wounds, Aggregate 5 (2024) e493.
[27] V. Brillo, L. Chieregato, L. Leanza, S. Muccioli, R. Costa, Mitochondrial dynamics, ROS, and cell signaling: a blended overview, Life 11 (2021) 332.
[28] S. Willenborg, D.E. Sanin, A. Jais, X. Ding, T. Ulas, J. Nüchel, M. Popović, T. MacVicar, T. Langer, J.L. Schultze, A. Gerbaulet, A. Roers, E.J. Pearce, J. C. Brüning, A. Trifunovic, S.A. Eming, Mitochondrial metabolism coordinates stage-specific repair processes in macrophages during wound healing, Cell Metabol. 33 (2021) 2398–2414.e9.
[29] W. Yu, Z. Wang, K. Zhang, Z. Chi, T. Xu, D. Jiang, S. Chen, W. Li, X. Yang, X. Zhang, Y. Wu, D. Wang, One-carbon metabolism supports s-adenosylmethionine and histone methylation to drive inflammatory macrophages, Mol. Cell. 75 (2019) 1147–1160.e5.
[30] Y.-T. Wang, A.J. Trzeciak, W.S. Rojas, P. Saavedra, Y.-T. Chen, R. Chirayil, J. I. Etchegaray, C.D. Lucas, D.J. Puleston, K.R. Keshari, J.S.A. Perry, Metabolic adaptation supports enhanced macrophage efferocytosis in limited-oxygen environments, Cell Metabol. 35 (2023) 316–331.e6.
[31] J. Huang, R. Yang, J. Jiao, Z. Li, P. Wang, Y. Liu, S. Li, C. Chen, Z. Li, G. Qu, K. Chen, X. Wu, B. Chi, J. Ren, A click chemistry-mediated all-peptide cell printing hydrogel platform for diabetic wound healing, Nat. Commun. 14 (2023) 7856.
[32] N. Mandakhbayar, Y. Ji, A. El-Fiqi, K.D. Patel, D.S. Yoon, K. Dashnyam, O. Bayaraa, G. Jin, K. Tsogtbaatar, T.-H. Kim, J.-H. Lee, H.-W. Kim, Double hits with bioactive nanozyme based on cobalt-doped nanoglass for acute and diabetic wound therapies through anti-inflammatory and pro-angiogenic functions, Bioact. Mater. 31 (2024) 298–311.
[33] S. Xu, S. Li, M. Bjorklund, S. Xu, Mitochondrial fragmentation and ROS signaling in wound response and repair, Cell Regen. 11 (2022) 38.
[34] G. Chen, F. Wang, X. Zhang, Y. Shang, Y. Zhao, Living microecological hydrogels for wound healing, Sci. Adv. 9 (2023) eadg3478.
[35] H. Liu, Y. Du, J.-P. St-Pierre, M.S. Bergholt, H. Autefage, J. Wang, M. Cai, G. Yang, M.M. Stevens, S. Zhang, Bioenergetic-active materials enhance tissue regeneration by modulating cellular metabolic state, Sci. Adv. 6 (2020) eaay7608.
[36] S. He, Z. Li, L. Wang, N. Yao, H. Wen, H. Yuan, J. Zhang, Z. Li, C. Shen, A nanoenzyme-modified hydrogel targets macrophage reprogramming-angiogenesis crosstalk to boost diabetic wound repair, Bioact. Mater. 35 (2024) 17–30.
[37] J. Zhang, G. Cao, L. Tian, J. Hou, Y. Zhang, H. Xu, M. Wang, Q. Jia, L. Wang, H. Yang, Intragastric administration of Pien Tze Huang enhanced wound healing in diabetes by inhibiting inflammation and improving energy generation, Phytomedicine 109 (2023) 154578.
[38] Z. Yang, K. Ren, Y. Chen, X. Quanji, C. Cai, J. Yin, Oxygen-generating hydrogels as oxygenation therapy for accelerated chronic wound healing, Adv. Healthcare Mater. 13 (2023) 2302391.
[39] Z. Yang, H. Chen, P. Yang, X. Shen, Y. Hu, Y. Cheng, H. Yao, Z. Zhang, Nano-oxygenated hydrogels for locally and permeably hypoxia relieving to heal chronic wounds, Biomaterials 282 (2022) 121401.
[40] R.A. Han, Y. Wu, Y.F. Han, X.F. Liu, H. Liu, J.C. Su, Engineered plant extracellular vesicles for autoimmune diseases therapy, Nano Res. 17 (2024) 2857–2873.
[41] Q.S. Kong, Z.M. Zhu, Q. Xu, F. Yu, Q.S. Wang, Z.H. Gu, K. Xia, D.W. Jiang, H. T. Kong, Nature-inspired thylakoid-based photosynthetic nanoarchitectures for biomedical applications, Small Methods (2023) 2301143.
[42] H. Chen, Y. Cheng, J. Tian, P. Yang, X. Zhang, Y. Chen, Y. Hu, J. Wu, Dissolved oxygen from microalgae-gel patch promotes chronic wound healing in diabetes, Sci. Adv. 6 eaba4311.
[43] R.M. Soo, J. Hemp, D.H. Parks, W.W. Fischer, P. Hugenholtz, On the origins of oxygenic photosynthesis and aerobic respiration in cyanobacteria, Science 355 (2017) 1436–1440.
[44] H. He, Q. Qin, F. Xu, Y. Chen, S. Rao, C. Wang, X. Jiang, X. Lu, C. Xie, Oral polyphenol-armored nanomedicine for targeted modulation of gut microbiota–brain interactions in colitis, Sci. Adv. 9 (2023) eadf3887.

[45] Y. Li, R. Fu, Z. Duan, C. Zhu, D. Fan, Construction of multifunctional hydrogel based on the tannic acid-metal coating decorated MoS_2 dual nanozyme for bacteria-infected wound healing, Bioact. Mater. 9 (2022) 461–474.
[46] K. Goldhahn, B. Kloesch, F. Aldawsari, C. Velazquez-Martinez, K. Schmetterer, G. Steiner, A7.11 Resveratrol and a resveratrol-salicylate hybrid molecule suppress cytokine production and proliferation of human CD4+T-cells, Ann. Rheum. Dis. 75 (2016). A60-A60.
[47] R. Ganugula, M. Arora, M.A. Lepiz, Y. Niu, B.K. Mallick, S.C. Pflugfelder, E. M. Scott, M.N.V.R. Kumar, Systemic anti-inflammatory therapy aided by double-headed nanoparticles in a canine model of acute intraocular inflammation, Sci. Adv. 6 (2020) eabb7878.
[48] M. Zhang, X. Zhang, T. Tian, Q. Zhang, Y. Wen, J. Zhu, D. Xiao, W. Cui, Y. Lin, Anti-inflammatory activity of curcumin-loaded tetrahedral framework nucleic acids on acute gouty arthritis, Bioact. Mater. 8 (2022) 368–380.
[49] P. Chen, X. Liu, C. Gu, P. Zhong, N. Song, M. Li, Z. Dai, X. Fang, Z. Liu, J. Zhang, R. Tang, S. Fan, X. Lin, A plant-derived natural photosynthetic system for improving cell anabolism, Nature 612 (2022) 546–554.
[50] J. Wei, G. Wang, F. Chen, M. Bai, Y. Liang, H. Wang, D. Zhao, Y. Zhao, Sol-gel synthesis of metal-Phenolic coordination spheres and their derived carbon composites, Angew. Chem., Int. Ed. Engl. 57 (2018) 9838–9843.
[51] D. Li, J. Li, S. Wang, Q. Wang, W. Teng, Dually Crosslinked copper-poly(tannic acid) nanoparticles with microenvironment-responsiveness for infected wound treatment, Adv. Healthcare Mater. 12 (2023) 2203063.
[52] Z. Fan, H. Zhou, P.Y. Li, J.E. Speer, H. Cheng, Structural elucidation of cell membrane-derived nanoparticles using molecular probes, J. Mater. Chem. B 2 (2014) 8231–8238.
[53] H. Zhao, Y. Huang, F. Lv, L. Liu, Q. Gu, S. Wang, Biomimetic 4D-printed breathing hydrogel actuators by nanothylakoid and thermoresponsive polymer networks, Adv. Funct. Mater. 31 (2021) 2105544.
[54] M. Bao, K. Wang, J. Li, Y. Li, H. Zhu, M. Lu, Y. Zhang, Q. Fan, L. Han, K. Wang, D. Wang, Y. Gao, B. Peng, Z. Ming, W. Liu, ROS Scavenging and inflammation-directed polydopamine nanoparticles regulate gut immunity and flora therapy in inflammatory bowel disease, Acta Biomater. 161 (2023) 250–264.
[55] Y. Jiang, X. Pan, M. Yao, L. Han, X. Zhang, Z. Jia, J. Weng, W. Chen, L. Fang, X. Wang, Y. Zhang, R. Duan, F. Ren, K. Wang, X. Chen, X. Lu, Bioinspired adhesive and tumor microenvironment responsive nanoMOFs assembled 3D-printed scaffold for anti-tumor therapy and bone regeneration, Nano Today 39 (2021) 101182.
[56] X. Wang, X. Sun, D. Gan, M. Soubrier, H.-Y. Chiang, L. Yan, Y. Li, J. Li, S. Yu, Y. Xia, K. Wang, Q. Qin, X. Jiang, L. Han, T. Pan, C. Xie, X. Lu, Bioadhesive and conductive hydrogel-integrated brain-machine interfaces for conformal and immune-evasive contact with brain tissue, Matter 5 (2022) 1204–1223.
[57] A.-W. Qiu, Z. Bian, P.-A. Mao, Q.-H. Liu, IL-17A exacerbates diabetic retinopathy by impairing Müller cell function via Act 1 signaling, Exp. Mol. Med. 48 (2016) e280-e280.
[58] P. Zhang, T. Li, X. Wu, E.C. Nice, C. Huang, Y. Zhang, Oxidative stress and diabetes: antioxidative strategies, Front. Med. 14 (2020) 583–600.
[59] Y. Min, D. Ahn, T.M.T. Truong, M. Kim, Y. Heo, Y. Jee, Y.-O. Son, I. Kang, Excessive sucrose exacerbates high fat diet-induced hepatic inflammation and fibrosis promoting osteoarthritis in mice model, J. Nutr. Biochem. 112 (2023) 109223.
[60] T.T. Nguyen, S. Wei, T.H. Nguyen, Y. Jo, Y. Zhang, W. Park, K. Gariani, C.-M. Oh, H.H. Kim, K.-T. Ha, K.S. Park, R. Park, I.-K. Lee, M. Shong, R.H. Houtkooper, D. Ryu, Mitochondria-associated programmed cell death as a therapeutic target for age-related disease, Exp. Mol. Med. 55 (2023) 1595–1619.
[61] Y. Guo, T. Guan, K. Shafiq, Q. Yu, X. Jiao, D. Na, M. Li, G. Zhang, J. Kong, Mitochondrial dysfunction in aging, Ageing Res. Rev. 88 (2023) 101955.
[62] M.E. Rivera, E.S. Lyon, M.A. Johnson, R.A. Vaughan, Leucine increases mitochondrial metabolism and lipid content without altering insulin signaling in myotubes, Biochimie 168 (2020) 124–133.
[63] C. Tokunaga, K.-i. Yoshino, K. Yonezawa, mTOR integrates amino acid- and energy-sensing pathways, Biochem. Biophys. Res. Commun. 313 (2004) 443–446.
[64] C. Dufour, S. Ravera, S. Cesaro, R. Bottega, C. Usai, C. Marco, A. Savoia, P. Degan, M. Faleschini, P. Cuccarolo, M. Columbaro, F. Corsolini, E. Cappelli, Shwachman-diamond syndrome: energetic stress, calcium homeostasis and mTOR pathway, Blood 126 (2015), 2410-2410.
[65] Z. Zhang, Q. Huang, D. Zhao, F. Lian, X. Li, W. Qi, The impact of oxidative stress-induced mitochondrial dysfunction on diabetic microvascular complications, Front. Endocrinol. 14 (2023).
[66] L. Liu, Y. Wu, K. Liu, M. Zhu, S. Guang, F. Wang, X. Liu, X. Yao, J. He, C. Fu, The absence of the ribosomal protein Rpl2702 elicits the MAPK-mTOR signaling to modulate mitochondrial morphology and functions, Redox Biol. 73 (2024) 103174.
[67] X. Jiang, W. Wang, J. Tang, M. Han, Y. Xu, L. Zhang, J. Wu, Y. Huang, Z. Ding, H. Sun, K. Xi, Y. Gu, L. Chen, Ligand-screened cerium-based MOF microcapsules promote nerve regeneration via mitochondrial energy supply, Adv. Sci. 11 (2024) 2306780.
[68] Y. Jiang, X. Zhang, W. Zhang, M. Wang, L. Yan, K. Wang, L. Han, X. Lu, Infant skin friendly adhesive hydrogel patch activated at body temperature for bioelectronics securing and diabetic wound healing, ACS Nano 16 (2022) 8662–8676.
[69] Y. Qian, Y. Zheng, J. Jin, X. Wu, K. Xu, M. Dai, Q. Niu, H. Zheng, X. He, J. Shen, Immunoregulation in diabetic wound repair with a photoenhanced glycyrrhizic acid hydrogel scaffold, Adv. Mater. 34 (2022) e2200521.
[70] Z. Yuan, J. Wu, Y. Xiao, H. Yang, S. Meng, L. Dai, P. Li, K. Cai, A photo-therapeutic nanocomposite with bio-responsive oxygen self-supplying combats biofilm infections and inflammation from drug-resistant bacteria, Adv. Funct. Mater. 33 (2023) 2302908.
[71] Z. Yang, Z. Yang, L. Ding, P. Zhang, C. Liu, D. Chen, F. Zhao, G. Wang, X. Chen, Self-adhesive hydrogel biomimetic periosteum to promote critical-size bone defect repair via synergistic osteogenesis and angiogenesis, ACS Appl. Mater. Interfaces 14 (2022) 36395–36410.
[72] Y. Ding, R. Ma, G. Liu, X. Li, K. Xu, P. Liu, K. Cai, Fabrication of a new hyaluronic acid/gelatin nanocomposite hydrogel coating on titanium-based implants for treating biofilm infection and excessive inflammatory response, ACS Appl. Mater. Interfaces 15 (2023) 13783–13801.
[73] Y. Kang, L. Xu, J. Dong, X. Yuan, J. Ye, Y. Fan, B. Liu, J. Xie, X. Ji, Programmed microalgae-gel promotes chronic wound healing in diabetes, Nat. Commun. 15 (2024) 1042.
[74] H. Wang, J. Cheng, F. Sun, X. Dou, J. Liu, Y. Wang, M. Li, J. Gao, X. Liu, X. Wang, F. Yang, Z. Zhu, H. Shen, L. Zhang, P. Tang, D. Wu, A super tough, rapidly biodegradable, ultrafast hemostatic bioglue, Adv. Mater. 35 (2023) 2208622.
[75] Z. Zhou, T. Deng, M. Tao, L. Lin, L. Sun, X. Song, D. Gao, J. Li, Z. Wang, X. Wang, J. Li, Z. Jiang, L. Luo, L. Yang, M. Wu, Snail-inspired AFG/GelMA hydrogel accelerates diabetic wound healing via inflammatory cytokines suppression and macrophage polarization, Biomaterials 299 (2023) 122141.
[76] Y. Guan, H. Niu, Z. Liu, Y. Dang, J. Shen, M. Zayed, L. Ma, J. Guan, Sustained oxygenation accelerates diabetic wound healing by promoting epithelialization and angiogenesis and decreasing inflammation, Sci. Adv. 7 (2021) eabj0153.
[77] Q. Yuan, J. Yin, L. Li, B. Bao, X. Zhang, M. Li, Y. Tang, Conjugated polymer composite nanoparticles augmenting photosynthesis-based light-triggered hydrogel promotes chronic wound healing, Adv. Sci. 11 (2024) 2304048.
[78] X. Han, C. Saengow, L. Ju, W. Ren, R.H. Ewoldt, J. Irudayaraj, Exosome-coated oxygen nanobubble-laden hydrogel augments intracellular delivery of exosomes for enhanced wound healing, Nat. Commun. 15 (2024) 3435.
[79] N. Liu, S. Zhu, Y. Deng, M. Xie, M. Zhao, T. Sun, C. Yu, Y. Zhong, R. Guo, K. Cheng, D. Chang, P. Zhu, Construction of multifunctional hydrogel with metal-polyphenol capsules for infected full-thickness skin wound healing, Bioact. Mater. 24 (2023) 69–80.
[80] J. Wu, W. Wang, J. Shen, N. Zhou, Y. Li, B.Z. Tang, M. Zhang, A thermosensitive hydrogel with efficient NIR photothermal conversion as injectable wound dressing for accelerating skin wound healing, Adv. Funct. Mater. (2024) 2312374.
[81] L. Feng, W. Shi, Q. Chen, H. Cheng, J. Bao, C. Jiang, W. Zhao, C. Zhao, Smart asymmetric hydrogel with integrated multi-functions of NIR-triggered tunable adhesion, self-deformation, and bacterial eradication, Adv. Healthcare Mater. 10 (2021) 2100784.
[82] Y. Wang, K. Liu, W. Wei, H. Dai, A multifunctional hydrogel with photothermal antibacterial and antiOxidant activity for smart monitoring and promotion of diabetic wound healing, Adv. Funct. Mater. (2024) 2402531.
[83] C.-Y. Wang, S.-C. Tsai, M.-C. Yu, Y.-F. Lin, C.-C. Chen, P.-C. Chang, Light-emitting diode irradiation promotes donor site wound healing of the free gingival graft, J. Periodontol. 86 (2015) 674–681.
[84] P.C. Chang, L.Y. Chien, Y. Ye, M.J. Kao, Irradiation by light-emitting diode light as an adjunct to facilitate healing of experimental periodontitis in vivo, J. Periodontal. Res. 48 (2013) 135–143.